MASTERS THESIS

Wave energy potential in the area of Sulafjorden and Breisundet

---

UNIVERSITY OF BERGEN

Geophysical Institute

Author: Benedicte Otterdal Nergaard

Supervisor: Birgitte Rugaard Furevik

Co-supervisor: Knut Barthel

January 20, 2020

Acknowledgements

I want to thank Birgitte Furevik, my supervisor, for the feedback and guidance throughout this thesis. Thank you for being available at all times, always answering my questions and for the motivating discussions around the topic of this thesis. Many thanks to Knut Barthel for having his door open, giving me valuable feedback and always answering my emails. I also want to thank Konstantinos Christakos for the last-minute proofreading and the much-appreciated feedback.

A special thanks to Silje, for always listening to my frustration, motivating me and just being there when needed. Thank you to the rest of my family and friends, outside and inside GFI for making studying bearable during all these years. Last, but not least a major thanks to my fiancé and rock, Øyvind, for always keeping me above water even when the water is rising. I would not have made it without you.

Benedicte O. Nergaard, January 2020

Abstract

This thesis investigates the wave climate and available wave energy in Sulafjorden and Breisundet, an area close to Ålesund on the Norwegian west coast. Data from the Simulating Waves Nearshore (SWAN) model for 2007-2017 and wave buoys operated by the Norwegian Public Road Administration (NPRA) for 2016-2018 is analysed in the search of the most accurate estimate of wave power in this area. Sulafjorden and Breisundet are characterised as a fjord exposed to open ocean. For Breisundet a positive trend in the winter months in significant wave height (H_s) is found to be 0.25 metres over 10.5 years. The wave energy flux (E_f) varies from 10.6 kW/m at Breisundet to 1.2 kW/m at the innermost site in Sulafjorden. Seasonal changes in the wave climate are characterising the investigated area, which affects the variation in E_f at all sites. SWAN is validated and compared with data from the NPRA buoys. To be able to conduct the validation of E_f, the wave period ratio (WPR=T_e/ T_{m02}) is found to provide a good estimate of the energy period in the E_f calculation for the NPRA buoys. T_e is not available from the buoy data set but it is necessary for wave energy estimations. WPR is found to provide the most accurate result for E_f if site specified values calculated from the SWAN wave spectrum are used. The result for WPR is found to be 1.5 at, Breisundet, the offshore site, and 1.9 at the innermost fjord site in Sulafjorden.

Contents

List of Figures

List of Tables

List of abbreviations

H_s Significant wave height

MET The Norwegian Meteorological Institute

NPRA Norwegian Public Road Administration

REC Runde Environmental Center

SWAN Simulating WAves Nearshore

WEC Wave Energy Converter

WMO World Meteorological Organization

WPR Wave Period Ratio, also named α

Chapter 1

Introduction

The ocean influences several important affairs regarding mankind. Affairs related to shipping, maritime travelling, health, industry and energy. And of course, the Earth's climate system. Knowledge about the blue part of our planet is hence of great significance. With the increasing population and changing climate, the need for non-polluting energy sources and food supplies is greater than ever. The ocean acts directly as an energy source, as host for the extraction of other energy sources such as wind-power and oil/gas fields, and as a food supplier. Predicting and modelling its physics and dynamics is crucial regarding all these affairs. The topic of this research is an important part of the ocean dynamics governing the motion of the ocean surface, namely ocean surface waves and its related wave energy. When describing ocean surface waves one of the most important variables is the wave height. Due to the impact of higher waves and for simplicity's sake, significant wave height (H_s) is the most used measure of wave height. H_s is defined as the average of the highest one-third of waves occurring in a record of typical 20 to 30 minutes duration.

Ocean surface waves, also known as surface gravity waves, are forced by wind where gravity is the restoring force. The wind speed, duration and fetch determine the wave evolution. High wind speed and long fetch over a long duration result in more energy from the wind being transferred to the water surface and a rougher sea state. Looking at global weather systems there are areas with a strong and constant supply of wind. In these areas it can be observed high waves which propagate away. Globally there are three areas known for producing a great amount of wave activity. Extra-tropical cyclone activity causes this activity. One zone is around Antarctica in the Southern Ocean where the mean annual significant wave height reaches 5 meters. The two other zones are found in the northern part of the Pacific Ocean and the Atlantic Ocean where the mean annual significant wave height reaches over 3 meters, as seen from the left side of figure 1.1 (Aarnes, 2015). The right side of figure 1.1 shows the corresponding annual mean wind speed for these areas and indicates the relation between wind speed and wave height.

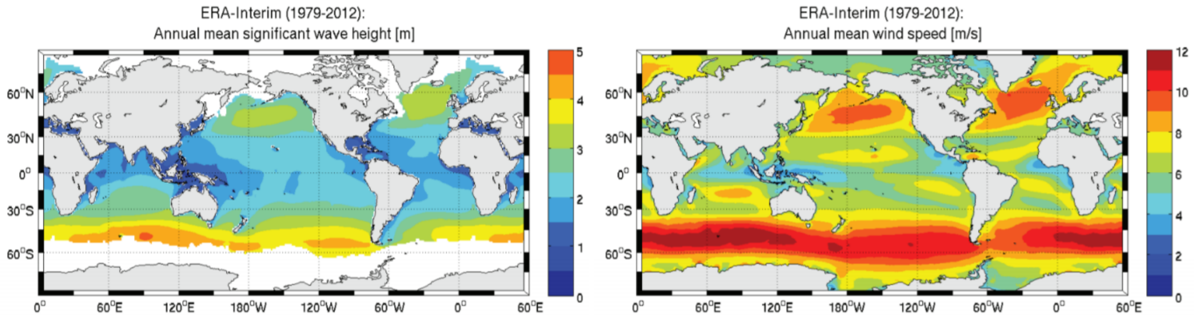

Figure 1.1: Annual mean significant wave height [m] (left panel) and annual mean wind speed [m/s] (right panel). Data based on ERA-Interim over the period 1979-2012. White areas in the left panel illustrate the maximum ice extent (Aarnes, 2015).

By analysing waves, information about the sea state, wave climate and the wave power can be retrieved. Sea state refers to the investigation of a shorter time period, whereas the wave climate at an area refers to long term description of the sea state. Waves carry a great amount of energy, and often over an extensive distance. Swimming on a beach and suddenly being hit by a wave indicates the power existing in the ocean. Knowledge about this amount, and to locate areas exposed to continuous wave activity, is of great interest both for offshore constructions and marine traffic. To be able to calculate the wave energy at a location it is necessary to have information about two wave parameters, H_s and the wave period. H_s is directly related to wave energy through its effect on potential and kinetic energy to the surface water particles. But how much energy does the ocean contain? Evaluating wind-generated surface waves the Intergovernmental panel on climate change (IPPC) has estimated the global total theoretical wave energy resource to be 32,000 TWh/yr (Edenhofer et al., 2012). A number revealing great potential as an energy source. The estimated mean power of wave energy for the different parts of the ocean is shown in figure 1.2. Areas of high mean power correspond to the result for high wind speed and wave height from figure 1.1.

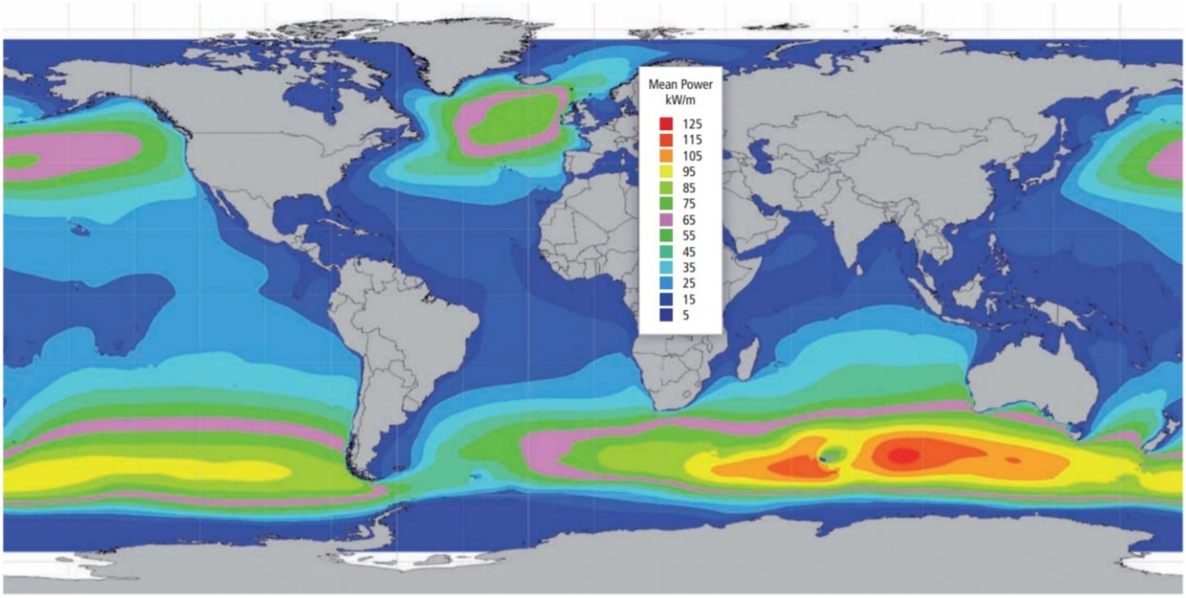

Figure 1.2: Global distribution of mean wave power [kW/m] (Edenhofer et al., 2012).

The estimate of the global theoretical wave energy resource is tremendous, but is only represented as a small portion of the already small part of the renewable contribution to the world energy mix (Edenhofer et al., 2012). This is due to the difficulties of extracting the energy from the ocean and turn it into electrical power. Immature technology limits the potential. Nevertheless, the world is facing the need for more available energy coming from renewable sources. The 'everything makes a difference' statement applies and most coastal countries are today researching and developing technology to extract ocean wave energy (Hemer et al., 2019). One of these countries is Norway, which is located close to the North Atlantic Ocean (Hemer et al., 2019). The wave climate at the Norwegian coast is typically split into offshore and fjord systems. A result of the latitude and its long coast, a combination of swell waves and wind-generated surface waves characterise both systems. Rough sea state defines the autumn and wintertime, whereas calmer conditions occur during summer and spring. Norway has the world's second-longest coastline for a single country, with 100,915 km (Thuesen et al., 2019). Despite this, monitoring and mapping the coast is not highly prioritised. Most of the information about the wave climate for the Norwegian coast comes from modelling. Only a few observational buoys are employed, and these have been implemented due to other reasons than to monitor the wave energy.

At Runde Environmental Center (REC), located on Runde Island close to Ålesund, a wave energy testing facility is found. This provides an interesting area for wave energy modelling. A wave energy converter (WEC) has been tested by the company Waves4Power at Runde (Waves4Power, 2019), making it interesting to verify that the surrounding area is suited for the use of WEC. By coincidence, one of the closest fjords, Sulafjorden, are being investigated for the implementation of a bridge. Several observational buoys have been deployed in this fjord due to this, and the logged data have been made available online by the Norwegian Meteorological Institute. The buoy data is obtained by FUGRO on demand from the Norwegian Public Road Administration (NPRA). To contribute to more available information about the wave climate and available wave energy here, this study investigates the wave energy potential and wave climate in Breisundet and Sulafjorden. The investigated area is shown in figure 1.3.

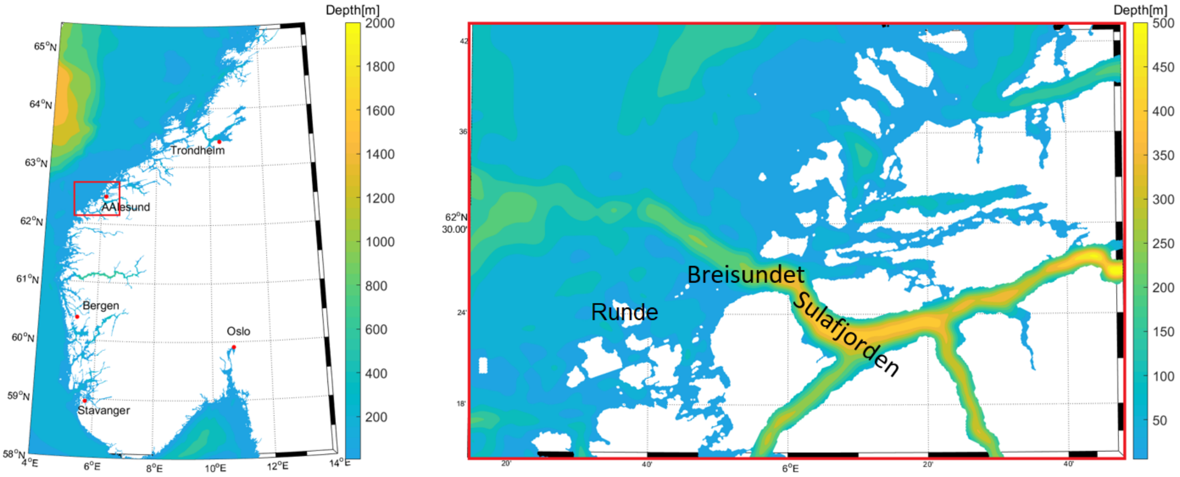

Figure 1.3: Left panel: Map of Southern Norway with the biggest cities, red rectangle framing the area of interest. Right panel: Map of the area of interest. Colorbar indicates depth in metres.

1.1 Outline

State of the art is elaborated in the section below followed by providing the necessary theory about waves, found in chapter 2. In chapter 3 information about the research area and some additional information about wave energy converters is given. Next, information about the analysed wave data is given in chapter 4 together with a validation of the data. In chapter 5 the methods used to process the data is described, leading up to chapter 6 where results from the wave analysis and wave energy calculations are given. Following the results is a detailed discussion in chapter 7. The thesis finishes with a conclusion based on the results and discussion, and proposed future work.

1.2 State of The Art

In 2017 renewables accounted for 18.1% of the total final energy consumption, whereas less than 2% of this amount came from wave energy (Appavou et al., 2019). Looking at the trend, both the renewable and wave energy part are growing (DNV-GL, 2019). Today, most of the ocean wave technology is at an early stage, but more literature on the topic is arising and several different studies have been and are being conducted (Hemer et al., 2019). Related studies include literature about wave climate and sea state to instrumentational testing of wave energy converters (WEC). Wave energy is presented as either potential, theoretical or practical estimate, or as a combination depending on the aim of the research.

For the Balearic Sea wave energy has been computed by using the spectral wave model WAM, forced by ECMWF ERA-Interim wind fields, together with observational buoys (Ponce de León et al., 2016). Good correlation between buoys and WAM data is provided, and for the Balearic sea, Ponce de León et al. (2016) find an energy flux raging from 9.1 kW/m to 2.5 kW/m with large spatial and temporal variability. For the Swedish west coast, the wave energy is calculated from wave data resulting from WAM and SWAN wave models calibrated with wave measurement buoys. One of the research sites included in the Swedish research (Waters et al., 2009), have a wave power plant installed. The result for the wave energy flux here ranges from 5.2 kW/m at an offshore site to 2.8 kW/m nearshore, and 2.4 kW/m in Kattegat (Waters et al., 2009). The European Marine Energy Centre Ltd. (2009) used information about wave energy provided from the Atlas of UK Marine Renewable Energy Resources, together with buoys and several models. This data was used to further understand the potential for wave energy generation in the UK with economic reasoning. The result is an assessment guide for wave energy resources, which provides techniques to determine how much wave energy is available for an area.

The path from waves to electrical power is long and advanced. A WEC needs to withstand high waves during storms when placed in traditional sites on a coast open to the sea and account for all the different directions the waves are coming from. However, the wave height during a storm is strongly reduced when considering a section from the open sea over the shelf and into the fjords. The outer parts of fjords and archipelago in Norway could, therefore, be interesting areas for small-scale WEC's with low investment costs and in combination with floating solar energy systems or fish farming. Before the deployment of a WEC at a location, the wave climate and available wave energy need to be researched and estimated. How will the theoretical wave energy vary throughout a year? Is the mean wave direction spread out? What are the values of the highest occurring waves? And, how little is the potential in low energy periods? These are questions which needs to be addressed in order to employ a WEC.

To be able to calculate wave energy it is necessary to have information about significant wave height and energy wave period. There are several sources of data which provide information about these variables as seen from the mentioned literature. Some data may not include the necessary wave variables. For the NPRA buoys, the energy period is not a part of the output and not possible to calculate. The energy period is therefore estimated by other variables. This is an interesting aspect as it will influence the accuracy of the wave energy estimate. Sulafjorden and Breisundet make an excellent area to analyse the available wave energy and the influence of different estimated wave periods, due to the access of modelled and observed data. With a WEC employed close to this area (Waves4Power, 2019), it is expected to see a high potential for wave energy close by as well.

All this leads up to the objectives of this research, where the main objective is to analyse and compare data from observational buoys and the Simulating Waves Nearshore (SWAN) model. By doing this it is possible to state the wave conditions and estimate the available wave energy for this area. A further look into the evolution of wave parameters from offshore and into the fjord is included with emphasis on obtaining the most correct estimate of wave energy period. Maximum wave height from SWAN and the NPRA buoys is also analysed and compared to see the wave evolution from the open ocean and into a fjord-system. For the energy period investigation and 'ocean to fjord evolution' a case study from SWAN is included with additional information from offshore sites.

Chapter 2

Fundamental Wave Theory

2.1 Assumptions and Basic Definitions

When the ocean surface, initially at rest, is disturbed, conservation of mass and energy makes this disturbance travel and waves are created. Three forces interact in this action. One generating force, wherein the case of ocean surface waves the generating force is wind. Gravity/buoyancy and surface tension act as restoring forces, then inertia makes the wave overshot its equilibrium and the wave propagates. Waves can be characterised by different features but is typically characterised by their period. The waves in this paper are defined by a period of 1/4 – 30s, and their wavelength varies from 0.1 to 1500 meters (Holthuijsen, 2010).

Ocean surface waves caused by wind is one of the most obvious air-sea interactions known (Janssen et al., 2013). Pressure fluctuations created by the wind causes a transfer of energy from the wind to the water. The pressure fluctuations are in resonance with the waves; pushing down water particles on the way down, and suction of water particles on the way up (Ryszard, 1996). The wind sets the surface water particles in motion, which then act through friction with the underlying layers and lateral particles. The water particles will move in the vertical with a circular motion, as simplified in the schematic figure 2.1. A true surface is random and chaotic, not symmetrical. To be able to predict and analyse a surface consisting of several waves travelling in different directions and with different speed and length, the wave behaviour needs to be theorised. The result is a model describing this behaviour.

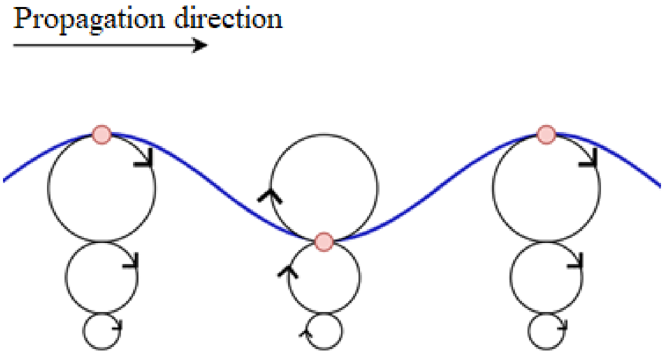

Figure 2.1: Simplified schematic figure of the vertical motion of water particles.

To be able to describe the motion of waves mathematically a few assumptions are made: the fluid is inviscid, incompressible and the fluid flow is irrotational (Laing et al., 1998). From this, a wave can be presented as a simple sinusoidal, long-crested, progressive wave with periodic motion (figure 2.2) (Laing et al., 1998).

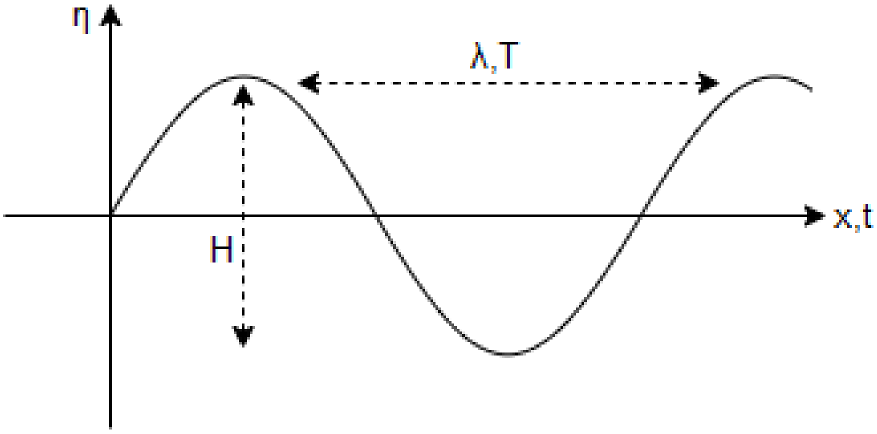

Figure 2.2: Schematic figure of a sinusoidal wave with relevant wave parameters.

Several definitions characterise the wave depicted in figure 2.2:

- $\eta(x, t)$ = the instantaneous vertical displacement of the sea level.
- Wavelength λ = the distance from crest to crest (or through to through).
- Wave period T = the time interval between two arriving crests.

- Frequency f = $\frac{1}{T}$, measured in numbers per second (Hz).
- Amplitude a = size of the maximum displacement from mean sea level (η=0)=H/2.
- Wave height H = difference in elevation from crest to through (=2a).
- Phase speed c = the rate of propagation

The sinusoidal, long-crested, progressive wave from figure 2.2 is mathematically described as:

$$\eta(x,t) = a\sin(kx - \omega t), \tag{2.1}$$

Where $k = \frac{2\pi}{\lambda}$ is the wavenumber (measure of number of crests per distance) and $\omega = \frac{2\pi}{T}$ is the angular frequency (number of radians per second). As equation 2.1 is a periodic and progressive wave the wavelength can be expressed as $\lambda = cT$. Equation 2.1 can also be written as:

$$\eta(x,t) = a\sin(\frac{2\pi x}{\lambda} - \frac{2\pi t}{T}) \tag{2.2}$$

or in terms of phase speed:

$$\eta(x,t) = a\sin[k(x - ct)] \tag{2.3}$$

According to equation 2.1 the sea level varies in space (x) and time (t), and has the same form above and below mean sea level. In reality, this is not the case as the crests are sharp and shorter than the longer and flatter troughs, but the equation provides a good starting point for understanding surface waves (Laing et al., 1998). The equation tells only about one wave, whereas the true surface consists of many waves travelling with different speeds and wavelengths.

Searching the dynamic relation between wave period T and wavelength L the linear theory of a right-travelling wave at the surface with a flat bottom at depth z=-h is applied. Approximating and finding the solution to the linearized equations of motion with boundary conditions for small amplitude waves ($a/\lambda \ll 1$) the dispersion relation is found:

$$\omega^2 = gk\tanh(kh) \tag{2.4}$$

The equation describes the relation between wave number and wave frequency. From the dispersion relation (equation 2.4) the phase speed can be rewritten as:

$$c^2 = \frac{\lambda^2}{T^2} = \frac{\omega^2}{k^2} = \frac{g}{k}\tanh(kh), \tag{2.5}$$

resulting in the phase speed being dependent on wave number (g is the gravitational acceleration).

By approximating the dispersion relation (equation 2.4) the solutions for long and short waves are provided. The ratio between wavelength and water depth (λ/h) indicates if the waves are referred to as short or long (Dhanak and Xiros, 2016). The vertical motion related to the water particles decreases with depth, and below a certain depth, the movement at the bottom is negligible. This depth corresponds to $h = \lambda/2$. But as long as the water depth is greater than $h > \lambda/4$ the bottom is not 'felt', and hence the water is referred to as deep. The transition zone from deep to shallow water accounts for water depth to be $\lambda/25 < h < \lambda/4$. Shallow water is characterised with $h < \lambda/25$. With $h < \lambda/$ the waves start to feel the bottom. A wave reaching the coast with decreasing depth will experience a decrease in wave speed and wavelength, whereas the period remains constant and the wave height increases (Laing et al., 1998).

With $h > \lambda/4$ the tanh kh term goes toward unity and the phase speed reduces to: $c = \sqrt{\frac{g}{k}}$. Having the relative water depth to be $h < \lambda/25$, the water is shallow ($tanhkh \rightarrow kh$), and the shallow water dispersion reduces to $c = \sqrt{\frac{g}{k}kh} = \sqrt{gh}$. From this it is seen that shallow water waves are non-dispersive. To characterise the speed of several waves the term group speed is used. In general group speed is defined as $c_g = \frac{d\omega}{dk}$. Using this on the above definitions the group velocity for deep water waves is $c_g = \frac{c}{2}$ and for shallow water waves $c_g = c$. For intermediate depths $c_g = \frac{c}{2}(1 + \frac{2kh}{\sinh 2kh})$ (Dhanak and Xiros, 2016).

2.2 Coastal Impact on Waves

When the waves enter shallow water and start to feel the bottom, different phenomenons occur. Namely refraction, diffraction and shoaling. In the above section, it is mentioned that the wave height increase when waves enter shallower water. This is a result of preserving energy and is called shoaling. Eventually, when the wave reaches the coast the shoaling might lead to breaking of waves.

Refraction is another phenomenon related to the changing water depth. Imagine a wave travelling parallel with the coastline on different water depths. The segment of the wave travelling in the shallower water will travel slower than the rest of the wave. This will lead to a turning of the direction of the wave propagation and is why all waves entering the land is seen to be travelling straight into it. The last phenomenon to mention is diffraction. This occurs when waves encounter some sort of surface obstacle. The energy is then transformed along the wave crest and impacts the lee of the structure.

2.3 Complete wave fields from generation to evolution

The sea state at one area consist of a mix of different waves which have originated somewhere else and/or at that spot. Factors like water depth, wind speed, ocean fetch and duration of the wind event have an impact, as mentioned, on the wave growth and evolution. At the origin of a wave, the wind has started to blow. The first thing to appear are capillary waves ($\lambda < 1.7cm$ and $T < 0.1s$) (Dhanak and Xiros, 2016). If the wind keeps steady or increases, these capillary waves grow. Depending on the fetch, additional higher waves are generated (wind sea) as the energy moves from short to longer and longer waves. These waves are set to propagate, and when no longer affected by the originating wind the waves are called swell. The wind sea is typically short-crested, whereas swell waves are long-crested and often sinusoidal. The superposition of all waves in an area makes out a wave field, consisting of waves travelling with different wavelengths and in different directions.

2.4 The Wave Spectrum

Describing the sea state consisting of the mentioned waves is not straight forward. The ocean does not consist of simple sine waves but is a rather chaotic system of waves with different periods and wavelengths. With this chaotic state and the randomness arising, the description of the sea state at one point is dependent on statistical measures. The most typical statistical measures are H_s (significant wave height) and the mean zero down-crossing period T_{m02}, or other wave periods. A wave record (sea surface elevation over time) typically consists of information about these parameters. Analysing this record more detailed wave information is obtained. By Fourier transforming the record into different sine components approximations for the phase, amplitude and frequency is obtained for each component (Laing et al., 1998):

$$\eta(t) = \eta_0 + \sum_{j=1}^{N} a_j \sin(j\omega_0 t + \phi_j) \tag{2.6}$$

where:

- $\eta(t)$=sea surface elevation at time t
- η_0=mean surface level
- j=the number of wave component
- N=the total number of components
- a_j=the amplitude of the jth component
- ω_0=angular frequency of the longest wave fitted to the record
- ϕ_j=the phase angle of the jth component

The sum of all the different wave components makes up the wave spectrum, which gives the distribution of wave energy over frequency. By plotting the amplitude versus frequency, the amplitude spectrum is obtained. Instead of distributing the amplitude, the variance of each wave component is used. This is due to the statistical properties which variance holds, as well as the proportionality to the energy of the waves. With the assumption of having a stationary and Gaussian process, the variance density spectrum decides the statistical characteristics. The variance of the surface elevation is 1/2 the square of the wave amplitudes. Plotting each wave-variance component against frequency results in the function called the variance spectrum, S(f). This spectrum does not represent the true surface with all frequencies, this spectrum presents only the frequencies of $f_i = \frac{i}{D}$. By dividing the variance of the spectral component with the corresponding frequency interval $\triangle f = \frac{1}{D}$ the variance-density spectrum, E(f), is obtained. But still, this spectrum does not represent the true surface as it is based on discrete frequencies. Having the width of the frequency band $\triangle f$ to reach zero a continuous spectrum is attained. This is the continuous one-dimension variance-density spectrum, formulated in the equation 2.7 below (Holthuijsen, 2010). Synonymous this spectrum can be referred to as power spectral density and frequency spectrum.

$$E(f) = \lim_{\triangle f \to \ 0} \frac{1}{\triangle f} E \frac{1}{2} a^2 \tag{2.7}$$

It is more common to use the energy density spectrum due to the difficulty to grasp the meaning of the variance density spectrum. If the variance density spectrum is multiplied with ρg, the energy density spectrum is attained. The energy density spectrum relates the wave energy to frequencies. The form of the spectrum gives information about the wave field. For regular waves, the spectrum would turn out quite narrow, while irregular waves would result in a wider spectrum shape. The amplitude-phase model is one-dimensional, but the wave direction can easily be added by expanding the amplitude-phase model to include a directional dimension. The now three-dimensional amplitude-phase model sums harmonic waves in both x, y and t-space. By looking at the units for the added directional parameters the three-dimensional model reduces to a two-dimensional model in terms of frequency and direction. Applying the same method as above with the one-dimensional model, the result is the continuous two-dimensional variance density spectrum, given in equation 2.8:

$$E(f,\theta) = \lim_{\triangle f \to 0} \lim_{\triangle \theta \to 0} \frac{1}{\triangle f \triangle \theta} E \frac{1}{2} a^2 \tag{2.8}$$

Figure 2.3 shows an example of a two-dimensional wave directional spectrum from the wave model WAM4 with corresponding wave-variance spectrum.

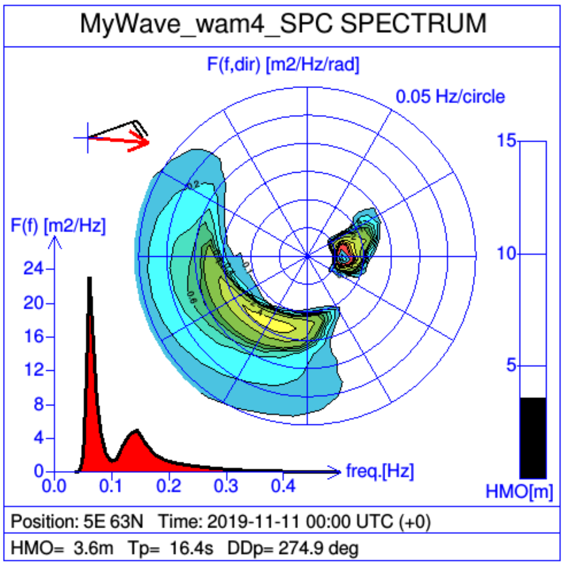

Figure 2.3: Two-dimensional wave directional spectrum example from WAM4 with corresponding wave-variance spectrum (Furevik, B 2019).

Regarding the shape of the spectrum, it can indicate what wave systems are present. If the wave system consists of both swell and wind sea the spectrum will show this. Wind sea and swell are usually well separated due to the different frequency they inhabit. Swells are quite regular long-waves where wind sea is the opposite. A wave spectrum can be as depicted in figure 2.4, where the peak at low frequency relates to swell and the second peak with higher frequency relates to wind sea. In cases of wind sea without swell, the peak referring to wind sea would quickly grow to be bigger than the peak representing swell.

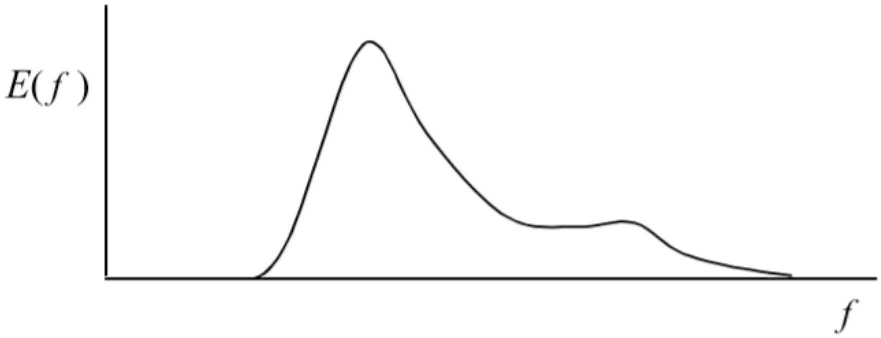

Figure 2.4: Schematised example of the continuous variance density spectrum (Holthuijsen, 2010).

2.4.1 Parameters and moments retrieved by the wave spectrum

Describing the statistical characteristics obtained by the wave spectrum, the term moment is used. Moments relate to the form of the wave spectrum and have a statistical meaning and is given as:

$$m_n = \int_{\infty}^{0} f^n E(f) df \tag{2.9}$$

Where E(f) is the variance-density spectrum. n=0 equals the area under the spectral curve. This represents, as defined by the World Meteorological Organization (WMO), the total variance of the wave record obtained by the sum of the variances of the individual spectral components (Laing et al., 1998). The first moment (n=1) defines the average of the deviations from a given value. The second moment(n=2) is then the average of the squares of the deviations about this same value. Higher orders of moments are then represented as a cube, and so on. By increasing the number of the moment the higher frequencies are weighted, meaning different parts of the spectrum is weighets. Weighting higher frequencies imply taking more of the end of the curve into account, where less energy is situated. Negative order of moments weighs lower frequencies. From the variance-density spectrum the significant wave height and different wave periods can be derived by the definition of moment (equation 2.10, 2.11, 2.12, 2.13 and 2.14).

$$T_p = f_p^{-1} \tag{2.10}$$

$$H_{m0} = \sqrt{2}\sqrt{\frac{8E}{\rho_w g}} = 4\sqrt{m_0} \tag{2.11}$$

$$T_{m01} = \frac{m_0}{m_1} \tag{2.12}$$

$$T_{m02} = \sqrt{\frac{m_0}{m_2}} \tag{2.13}$$

$$T_{m-10} = \frac{m_{-1}}{m_0} \tag{2.14}$$

Where E is identified as the total energy for a wave. Equation 2.12, 2.13 and 2.14 are defined, in order, wave period corresponding to the mean frequency of the spectrum, sea surface mean wave period and energy period. T_{m02} is an estimate of the mean zero down crossing period. The energy period, T_{m-10}, is an estimate of the most energetic part of the spectrum. f_p is the wave frequency for the peak of the spectrum. Equation 2.10 is the peak period. Peak period relates to the period of the most energetic waves. With an assemblage of theoretical results and measured spectra, different idealised spectrum shapes have been developed to represent different sea states (Laing et al., 1998). Under certain conditions, the spectrum can have a universal shape. The most used and known spectral models are the Pierson-Moskowitz and the JONSWAP spectrum (Pecher and Kofoed, 2017), where the Pierson-Moskowitz spectrum describes a fully developed sea (Pierson Jr and Moskowitz, 1964) and the JONSWAP spectrum describe waves in a growing phase (Hasselmann et al., 1973).

2.4.2 Wave Energy

As waves pass through a section of water, the water particles experience a change in elevation and in the horizontal. This movement represents changes in potential and kinetic energy. With water particles being moved up and down work is done against gravity referring to potential energy. Whereas the general movement in all directions refers to kinetic energy.

Considering a chunk of water with thickness $\triangle z$, the sudden potential energy with horizontal area $\triangle x \triangle y$ then equals $\rho g z \triangle x \triangle y \triangle z$. ρ is the water density, taken to be constant at 1025 kgm^{-3} and the gravitational acceleration to be 9.81 ms^{-2}. The potential energy for the whole water column will then equal the potential energy due to waves minus the potential energy in the absence of waves, equation 2.15. By time-averaging and considering a harmonic wave with amplitude a (with the surface displacement being represented by equation 2.1) the corresponding equation for the potential energy is then per unit surface area:

$$E_{potential} = \overline{\int_{-d}^{\eta} \rho g z dz} - \overline{\int_{-d}^{0} \rho g z dz} = \overline{\int_{0}^{\eta} \rho g z dz} \tag{2.15}$$

$$E_{potential} = \overline{\frac{1}{2} \rho g \eta^2} = \frac{1}{4} \rho g a^2 \tag{2.16}$$

For the same chunk of water the sudden kinetic energy equals $\frac{1}{2}\rho \triangle x \triangle y \triangle z u^2$, with $u^2 = u_x^2 + u_z^2$. Again considering the whole water column and time-averaging, the kinetic energy per unit surface area equals:

$$E_{kinetic} = \overline{\int_{-d}^{\eta} \frac{1}{2} \rho u^2 dz} \tag{2.17}$$

Solving the integral from equation 2.17 for the same harmonic wave the kinetic energy induced by a wave results in equation 2.18

$$E_{kinetic} = \frac{1}{4} \rho g a^2 \tag{2.18}$$

With the theory of total energy = potential energy + kinetic energy, the total time-averaged wave energy is then given by (where H is the wave height):

$$E_{total} = \frac{1}{2} \rho g a^2 = \frac{1}{8} \rho g H^2 \tag{2.19}$$

As the wave passes the wave energy is transported. In relation with available wave power, it is the energy transport (or energy flux) which is of importance. The energy flux per length along the wave crest is defined as:

$$E_f = c_g E, \tag{2.20}$$

and has units of W/m. In the case of deep water the group velocity can be written as $c_g = \frac{g}{2\omega} = \frac{g}{f4\pi}$. The total energy written in terms of the energy spectrum (S(f)) can be written as:

$$E_f = \rho g \int_0^\infty S(f)df. \tag{2.21}$$

The wave energy flux can be expressed by using the definitions for significant wave height (equation 2.11) and energy period (equation 2.14) in terms of spectral moments for deep water (Varlas et al., 2017):

$$E_f = \frac{\rho g^2}{4\pi} \int_0^\infty \frac{S(f)}{f} df = \frac{\rho g^2}{4\pi} m_{-1} \tag{2.22}$$

$$E_f = \frac{\rho g^2}{4\pi} T_{m-10} m_0 = \frac{\rho g^2}{64\pi} T_{m-10} H_{m_0}^2 \tag{2.23}$$

Wave energy flux gives the mean transport rate of wave energy through a vertical plane (parallel to the wave crest). Providing a good estimate of the available energy, in the units of watts per meter of wave crest length. Higher values of H_s and T_{m-10} results in higher values of E_f, and E_f is more sensitive to changes in H_s than to changes in T_{m-10}.

The wave energy period T_{m-10} may not always be an available parameter from the data sets, but there are different ways to calculate or estimate it. Depending on what wave parameters are available, most methods involve using other wave period measures such as T_p, T_{m01} or T_{m02} and relating these to T_{m-10} by multiplying by a factor. One method calculates the energy period from the constant α and T_{m02} (Cahill and Lewis, 2014). Where the α varies depending on the area and the researched wave field. Equation 2.24 shows the relation.

$$T_e = \alpha_B T_{m02} \tag{2.24}$$

2.5 Obtaining Wave Information

A wave record presenting wave characteristics at one location is normally presented as sea surface variations over time. To obtain this wave record different methods are used. In-situ measures done by buoys or modelled wave conditions are two of these methods.

2.5.1 In-situ Buoy Measurements

Depending on how many buoys are used and how well they are spread, they provide information locally about the wave conditions. Information about wave height, wave direction and the wave frequency are some of the typical output variables. Different wave-buoys measure these parameters with different techniques. The most typical method is that the buoys follow the motion of water particles by floating at the ocean surface, and measures the vertical acceleration the instrument has. The vertical acceleration is integrated twice to obtain vertical motion as a function of time (Holthuijsen, 2010).

The wave record obtained by buoys has a tendency to look more symmetrical than reality. Wave crests and throughs cover different sized area above and below the mean level, the crest tends to be sharper and the throughs flatter. The symmetrical appearance is due to a slight horizontal movement of the buoys when being hit by incoming waves. The reaction time of the buoy affects the wave record, for example regarding a very steep and/or fast wave, the water will flush over the instrument in such a speed making it not possible to retrieve the maximum wave height and influencing the frequency interval the buoy measures. The data signal logged by the buoy is sent to receiving stations either on platforms or land via radio communication and is tracked by the Global Positioning System (GPS) (Holthuijsen, 2010).

2.5.2 Modelling Waves: Simulating Waves Nearshore (SWAN)

The size and remoteness of the ocean make it difficult to have buoys covering every area of interest. For wave forecasting or retrieving wave information from a wide area one often turns to modelling. Today there are several models which calculate wave parameters. The Simulating Waves Nearshore model (SWAN) is one of these. SWAN is a third-generation spectral wave model which is developed at Delft University of Technology. The wave model is available for free as an open-source at http://www.swan.tudelft.nl (Booij et al., 1999). Being a third-generation model means all impacting physics is represented in the simulation. SWAN employs implicit propagation schemes, making it stands out from other wave models as the wave propagation is good for shallow water and coastal regions. It is an extension of deep-water models such as WAM (WAMDI-Group, 1988) and WAVEWATCH III (Tolman, 1997). It can be shortly explained that SWAN simulates the wave spectra generated by wind.

In general, all third generation models solve the action balance equation (equation 2.25 is given in cartesian coordinates and applies for small scale applications (SWAN-Team et al., 2009)):

$$\frac{\partial N}{\partial t} + \frac{\partial c_x N}{\partial x} + \frac{\partial c_y N}{\partial y} + \frac{\partial c_\sigma N}{\partial \sigma} + \frac{\partial c_\theta N}{\partial \theta} = \frac{S_{tot}}{\sigma}. \tag{2.25}$$

Where N=E/σ is defined as the action density, E is the energy density and σ is the frequency. c is the group speed and propagation velocity. S_{tot} is the source and sink terms. Equation 2.25 is a conservation equation, where the total action is conserved unless there is some sort of input of wave action acting either as a sink or a source (S_{tot}). The equation also takes background currents into account. If no background currents are present, equation 2.25 reduces to the wave energy balance equation.

Different propagation, generation and dissipation processes can be accounted for in SWAN. Propagation processes such as diffraction, shoaling, refraction, propagation through geographic space, impacts of currents and obstacles. Dissipation and generation processes such as wind forcing, white-capping, depth induced wave breaking, dissipation by bottom friction and wave-wave interactions (SWAN-Team et al., 2009).

The term on the right side of equation 2.25 sums the contribution of six processes in shallow water (as defined by SWAN-Team et al. (2009)):

$$S_{tot} = S_{in} + S_{nl3} + S_{nl4} + S_{ds,w} + S_{ds,b} + S_{ds,br} \tag{2.26}$$

where the different terms express wave growth by the wind (S_{in}), nonlinear transfer of wave energy through three-wave(S_{nl3}) and four-wave interactions(S_{nl4}) who accounts for the transport of energy between the frequencies and wave decay due to white-capping ($S_{ds,w}$), bottom friction($S_{ds,b}$) and depth-induced wave breaking($S_{ds,br}$) which both dissipate the waves. These processes act as either wave generators or wave decaying, and are represented by semi-empirical approximations. SWAN calculates the action balance equation and propagates the solution forward in time. The waves are described by the two-dimensional energy density spectrum $E(f, \theta)$. The two-dimensional spectrum accounts for the wave boundary and initial conditions.

Running SWAN

In order to run the SWAN model, different input data needs to be provided, such as wind input, wave spectra on the open borders and bathymetry data, as the model is driven by these. The choice of computing on regular, curvilinear or unstructured grid is made, and if the cartesian or spherical coordinate system should be used. It is optionally either stationary or non-stationary (SWAN-Team et al., 2009). The numerical propagation scheme is implicit for SWAN and is why it is so widely used in shallow waters. Different choices of output parameters are made based on the research. Running SWAN produces 2D wave information fields and spectra for chosen positions. Many of the processes that affect wave conditions vary in both time and space, hence for the wave information to be correct numerical models which acquire for these needs to be used.

Besides wave spectra at the edge, wind input and bottom conditions, the grid needs to be chosen, including nesting. Regarding the grids, these can either be structured or unstructured. In this research, the grid is structured. Two nests are used in this research, one coarse over a larger region and one finer for the smaller region. The wave computation is first done for the larger region, and then on the finer scale by the information form the coarser nest resulting in greater resolution. The boundary conditions on the small area are then generated by the computation from the coarser grid. For the computation different spatial and spectral grids need to be provided. The spectral grid is where the models perform the computations. Whereas the spatial grid needs to include a computational spatial grid, one spatial input grid and one spatial output grid. The input provides information about bathymetry, water level, bottom friction, wind etc. The output grid gives the result of the computation.

Chapter 3

Background Information

3.1 Wave Energy Converters (WEC)

The global total theoretical resource is estimated to be 32,000 TWh (Edenhofer et al., 2012). To capture and convert this energy to electrical power a Wave Energy Converter (WEC) is required. As of today, there are different ways of characterising the different types. Following the characterisation done by Aderinto and Li (2018), three categories are used: Oscillating Water Columns, Oscillating Body Systems, and Overtopping Converters wave (Aderinto and Li, 2018). The design differs in the effort to absorb as much energy as possible. WEC instruments are either fixed to the bottom or constructed as floating/submerged devices. Deployment of WEC is not widely done due to immature technology. The WEC needs to withstand heavy seas and storms, biofouling and the impact saltwater makes on the instrument. This issue is again related to the economy, as it is expensive to produce and develop wave energy converters (Aderinto and Li, 2018).

The efficiency of WEC depends on the design of the instrument. The wave energy needs to be captured by the device, converted to electricity and transported to land. The energy is going through multiple conversions (primary energy conversion with energy in working fluid, through a turbine and ending in an electrical generator). Through these conversions, there is energy loss (Falnes, 2002). The amount of the available wave energy being converted to electricity can be estimated by the annual energy production (AEP) of a WEC. Dhanak and Xiros (2016) provides the AEP to be:

$$AEP = P_{wave} \times width_{absorber} \times \eta_{w2w} \times availability \times hours_{annual} \tag{3.1}$$

P_{wave} is the mean wave power level, the second term is the width of the absorber. The third term is wave-to-wire efficiency, and then the last two terms are the wave energy availability and the yearly production hours. A good WEC needs to be able to extract energy from waves of different sizes and which are travelling in multiple directions. The depth at which the WEC is deployed at impacts the power capturing, depending on the instrument (Folley et al., 2005).

To begin with, when investigating the deployment of a WEC, the wanted area needs to be characterised by the wave climate. From this, it is possible to locate an attractive position for the instrument. Before deployment, the instrument needs to be calibrated to fit the wave conditions (the typical wave height of the area with the corresponding amount of energy). Employing a wave power farm also demands the construction of infrastructure, which is costly and time demanding. The most constant supply of waves are found in the open ocean, and the further away from land the more expensive the development and infrastructure will be. This, the harsh environment it needs to handle and the immature technology all are reasons for why the cost of developing wave farms is so high, and why little construction is being done. An advantage of WEC is the possibility of equipping the instrument with other practical instruments such as weather stations, mooring systems and electricity cables and so on. It is also possible to deploy a WEC in relation to ocean farms to make the farm less dependent on cables to land.

3.2 Sulafjorden and Breisundet

Sulafjorden is a fjord in the county of Møre and Romsdal, close to Ålesund. It flows past the two islands Sula and Hareid, where high mountains rage with altitude reaching 700m. The fjord is found at latitude 62.38 and longitude 6.09, stretches about 9 km and is 4-5km wide. The greatest depth is 445 meter and is found in the middle part of the fjord. The fjord ends in Breisundet which empties out in the open ocean. From Sulafjorden a subsurface valley, reaches far out in the open ocean (figure 3.1). The area of Breisundet is known as an area of choppy waves and heavy sea. Nautical charts from the Norwegian Mapping Authority warns about dangerous waves occurring in this area (Norwegian-Mapping-Authority, 2019). The waves from the open ocean enter Breisundet by moving through this valley with steep sides.

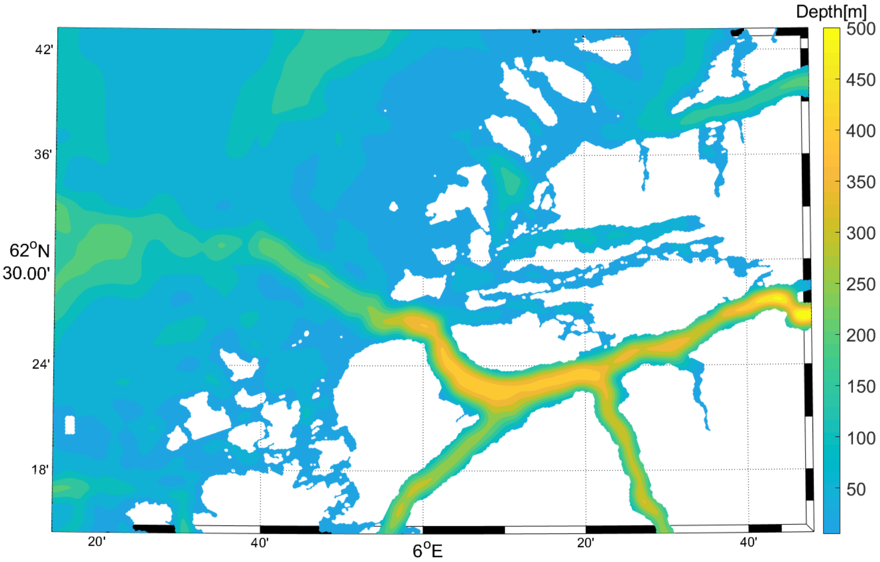

Figure 3.1: Map of Sulafjorden and Breisundet with color showing water depth in metres.

Typical coastal climate with changing seasons characterise the climate at this latitude. The autumn and winter months are dominated by storms and low temperatures, whereas the summer is characterised by warmer and calmer conditions. It is expected to see this affecting H_s and the available wave energy. In regards of the wave direction it is expected that there are two main directions at Breisundet and Sulafjorden, one coming straight from the open ocean (from west-northwest) and into the fjord (swell and wind sea) and the other coming from inside the fjord but with lower intensity (wind sea).

Chapter 4

Data

The main source for data is wave measurements from NPRA buoys and model output from SWAN. Information about these data and the model input used in the wave analysis will be given in the two following sections.

4.1 SWAN

4.1.1 January 2007 - June 2017

From January 2007 through June 2017 wave parameters from SWAN are derived for Breisundet, Sulafjorden and the surrounding area. 14 spectra are included in the data set, whereas only three are used in detail, located at site A, B and D (figure 4.1). The data is provided by Birgitte Furevik.

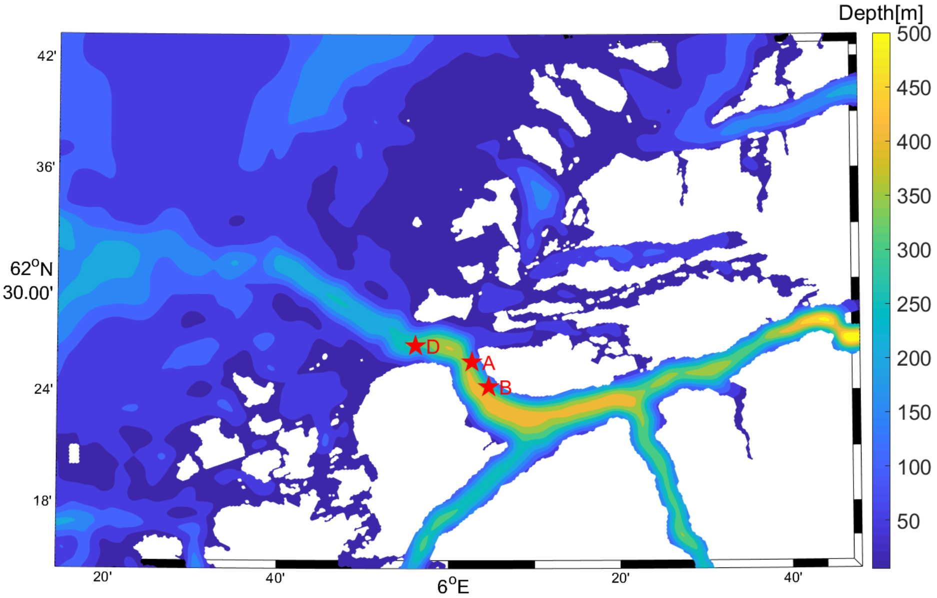

Figure 4.1: Map with marked (star symbol) positions of SWAN spectra and NPRA buoy locations, referred to as site A, B and D.

The model is run in non-stationary mode with spherical coordinates and wind varying in time and space. The computational input grid for the outer domain is 5.00-7.00°E and 62.00-64.00°N with the length of the grid cell in the x-direction of 3.1234°and y-direction length of 1.143°. All spectral wave directions are included, divided on 36 directions with 32 discrete frequencies with the lowest and highest frequency of 0.0464 Hz and 1.0 Hz. The outer domain has grid cells of 1 km x 1 km and nests the inner domain with grid cells of 250 m x 250 m. The result is 162 data points in x-direction and 128 in the y-direction. Bottom input is provided from the European Marine Observation and Data Network (EMODNET). The applied bottom friction physics is defined by the formulations done by Hasselmann et al. (1973).

The inner domain reaches 5.38°-6.73°E and 62.07°-62.57°N. Surface wind at 10 m above the surface from the atmospheric model WRF (Skamarock et al., 2008), downscaled to fit the spatial resolution 0.5 km, is applied as wind input to the model. For the boundary conditions at the grid boundaries for the outer domain, NORA10 hindcast with 3-hourly temporal resolution is applied. A nautical convention is used for the wind and wave direction, meaning the given direction will be in the direction where the waves are coming from. The sampling period of the model is set to every hour, and the output quantities are H_s, T_{m02}, T_{m01}, RTP, PDIR, DIR (defined in table 4.1). Table 4.2 shows the data specification for the spectrum data.

Output Quantity	Definition
H_s	Significant wave height
T_{m02}	Mean zero down crossing period
T_{m01}	Wave period corresponding to mean frequency from spectrum
RTP	Relative peak period
PDIR	Peak direction
DIR	Mean wave direction

Table 4.1: Defined output quantites from SWAN

Name	Location [Lat lon]	Start date	End date	Entries
SITE D	62.4405 5.9349	2007.1.1 00:00	2017.6.30 23:00	92016
SITE A	62.4275 6.0452	2007.1.1 00:00	2017.6.30 23:00	92016
SITE B	62.4026 6.0802	2007.1.1 00:00	2017.6.30 23:00	92016

Table 4.2: SWAN data specification

4.1.2 October 2016-December 2018

An additional SWAN data set for October 2016-December 2018 is used in the comparison and validation of SWAN and the NPRA buoys to have a longer time series to compare, enhancing the accuracy of the comparison. This SWAN run is conducted by Konstantinos Christakos and is run with the same specifications as the described data set above with WRF wind.

4.1.3 Case Study 24-28 December 2017

A SWAN run for 24-28th of December 2017 is carried out by the author to further understand the model and investigate the wave parameter evolution from the open ocean and into the fjord. The model is run with the same specifications as above but with additional spectrum points. Some of the spectra positions from the long SWAN-run (2007-2017) are used in this case study, some are removed and some additional sites are added. The location of the 11 spectra is shown in figure 4.2. The decision of choosing dates for the case study is to obtain wave information for some typical winter days without any storm impact. Start date 2017.12.24 00:00 and end date 2017.12.28 23:00, with one-hour time step. Site 7, 8 and 9 correspond to the same position as site D, A and B. This set provides useful wave information about both offshore systems and fjord systems.

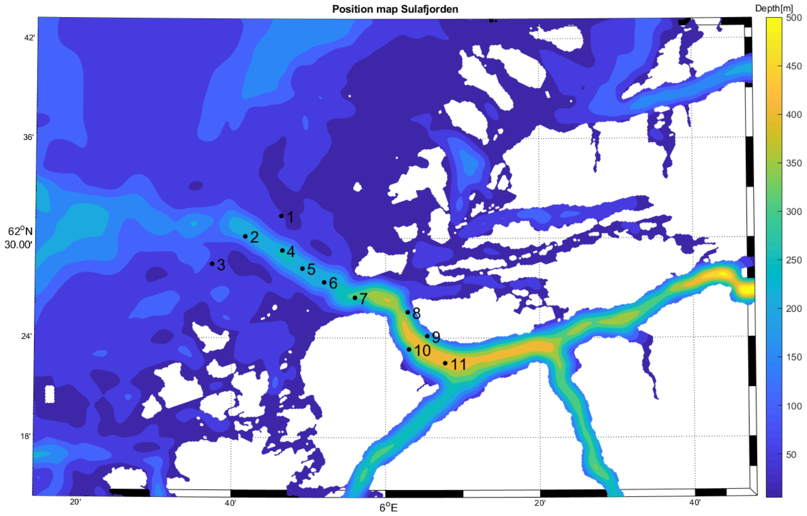

Figure 4.2: Map of the inner domain of SWAN case study December 2017. Spectrum points are numbered from 1 to 11, and colour indicate depth in metres below sea surface.

4.2 NPRA buoys October 2016-December 2018.

As a part of NPRA's work with 'Coastal Highway E39' several observational buoys are deployed in Sulafjorden and Breisundet. The buoys are operated by FUGRO, and provide wave and wind records. In the present work data from three SEAWATCH Wavescan buoys (Fugro, 2005) from this area is included. The positions of the buoys are the same as the SWAN spectra sites from figure 4.1 (site D, A and B). The data is available through MET(The Norwegian Meteorological Institute) Norway Thredds Service, at http://thredds.met.no/thredds/catalog/obs/buoy-svv-e39/catalog.html.

The SEAWATCH Wavescan buoys provide, among other parameters, information about significant wave height, periods, direction and frequency. This makes the buoy useful for validation of SWAN and further analysis of the wave conditions in Sulafjorden. The buoy is moored to the bottom at the different locations with the use of a slack mooring. See figure 4.3 for a schematic picture of the Wavescan buoy.

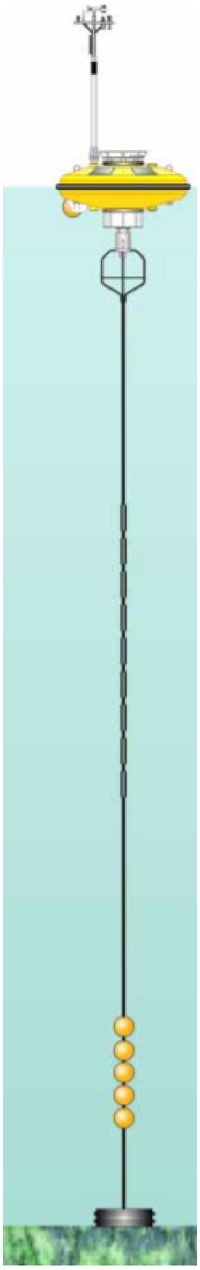

Figure 4.3: SEAWATCH Wavescan buoy (Fugro, 2005).

4.2.1 Frequency Range

SWAN and the NPRA buoys are set to operate on approximately the same frequency range. For both SWAN and NPRA buoys the high frequency is 1 Hz, but due to the configuration of the buoys, high-frequency waves are difficult to measure. The motion of the buoys gets a lag as the motion of the water is too fast for the buoys to respond. Over 0.5Hz the accuracy in which the buoys measure the wave spectrum decrease (Laing et al., 1998). When comparing different data-set one should be aware of this. A method for solving this issue is either to remove the higher frequencies (above 0.5 Hz) for the SWAN spectrum or add a high-frequency tale to the buoy data.

Chapter 5

Method

The software MATLAB is used for analysis for both the SWAN data and the NPRA buoy data. Analysis of significant wave height, wave periods, wind direction and wave direction is conducted by using statistics such as mean, maximum and minimum. Much of the data is represented by a time-series plot to best capture all the wave features occurring in the investigated period. To best represent the wave climate and the available wave energy, scatter energy diagrams are produced. This chapter describes the different methods the data is processed and calculated. All bathymetry maps are plotted with data from EMODNET.

5.1 SWAN validation

To validate the SWAN run, wave information from NPRA buoys are used for comparison. 27 months of data is compared. For the buoys, hourly measurements are taken out to correspond to the time-step of SWAN. H_s, T_{m02} and E_f is compared in scatter plots with corresponding regression lines for all sites (figure 6.4, 6.5 and 6.6). Due to the number of measurements, a quantile-quantile plot is added to better show the correlation. From the NPRA buoys spectrum information is not available and hence, T_e is not a given wave parameter. In this case, the relation from equation 2.24 is used. The estimation of the α value is described in the section below. The choice of using T_{m02}, and not T_{m01} or T_p is due to the definition of T_{m02}. T_{m02} is the mean wave period and closely related to the energy without the sensitivity T_p has. Time evolution of H_s, T_{m02} and E_f from both SWAN and

NPRA buoys are plotted together for each site to better indicate the deviation between the two data sets (figure 6.1, 6.2 and 6.3).

5.2 Wave energy period

In the validation of E_f from SWAN against the buoy data, the energy period needs to be estimated, as mentioned above. SWAN spectrum data for the corresponding time is considered in the search of α. The mean ratio of T_{m-10} to T_{m02} at site D, A and B are calculated. Providing three different α values which the energy period for the buoys for each site is estimated with.

The case study from SWAN provides additional investigation on the energy period. This is included to better understand the relation between T_{m-10} and T_{m02} and to give better estimates of E_f. Site D and B are considered as these represent one site close to the offshore system and one to the fjord system. Two cases are included. The first case includes fitted α values for both sites where α has been calculated from T_{m-10} and T_{m02} from spectra from site D (and the same for site B). The second case is the calculated mean *alpha* from all three sites. From this T_{m02} calculated with both options for site D and B are compared to T_{m-10} at these sites. The result from this, as seen in section 6.3, is the decision of using custom-fitted α values for all sites in the calculation of energy flux for the NPRA buoy data. Cahill and Lewis (2014) suggest the use of $\alpha = 1.2$, this value is too high for the fjord sites, and only used for the energy flux map plot to account for the offshore sea. After the case study, the whole SWAN time-series is investigated in the same matter to account for any seasonal changes or appearing trends.

5.3 Wave climate analysis

The wave climate is characterised by looking at variation and values for H_s, evaluating T_p and the wind speed and direction. Wave and wind roses at site D, A and B are included for SWAN and NPRA buoy data to show the variation in direction and the mean directions. The wind speed variation is plotted as a time-series to spot any seasonal changes, a mean filtered line is added to the plot to better depict the mean variation. All H_s values at site D for December, January and February from SWAN for 2007-2017 are extracted to analyse if any trend is seen in relation with increased storm activity. The data is averaged and standard deviated. A grouped mean bar plot is used, and a trendline is fitted to the data to depict any trend. Different mean two-dimensional plots for maximum H_s, mean H_s and mean T_p from SWAN for 2007-2017 is included to provide a better understanding of the whole research area.

5.4 Wave energy flux calculation

The different spectra from both SWAN-runs (2007-2017 and case study December 2017) are run through a MATLAB created function to calculate the spectral moments by equation 2.9. From this T_{m02}, T_{m-10} and H_{m0} is calculated by equation 2.13, 2.14 and 2.11. Equation 2.23 then calculates the corresponding wave energy flux. The annual wave energy transport is plotted in combined energy scatter diagrams, with the energy corresponding to H_s and $Te = T_{m-10}$ values. To retrieve values per year, all data is in advance divided on 10.5, corresponding to the length of the time-series. Constant lines of instant wave energy is added to the plot.

The analysis of seasonal changes of the mean wave energy for every month at site D is plotted as a 'boxplot', where different statistical measures are shown in one figure. All values from SWAN for 2007-2017 are included. Only site D is included as site A and B show the same trend but with smaller magnitudes and less variation in magnitude.

Chapter 6

Results

6.1 Validation of SWAN versus buoy measurements

Despite SWAN's good performance to describe wave parameters, a validation for the use of the model in Sulafjorden is included. Data from SWAN and the buoys are statistically analysed against each other to validate the quality and approve the use for this area. Site D, A and B are compared. The buoy data gives wave measurements from October 2016 to the end of December 2018. Accordingly, time-series from October 2016 to the end of December 2018 is taken out of the SWAN data from the data provided by Christakos. By doing this the model is validated for over more than two years, providing enough data to account for seasonal changes as well as for periods with instrumentational errors. The buoy provides measurements with recording for every 10 minutes, whereas the SWAN data provides one measurement per hour. Consequently, the buoy data is reshaped to only take out hourly measurements, to be able to compare the two different sources.

Time-series for the H_s, T_{m02} and E_f from SWAN and the NPRA buoys at site D, A and B are plotted together (figure 6.1, 6.2 and 6.3). The same variation is seen for SWAN and the NPRA buoys except for some cases. The difference between the two data sets is mostly seen from a deviation in magnitude. Statistical analysis shows good correlation for H_s (figure 6.4) for all sites. A slight decrease in correlation for the sites further into the fjord (figure 6.4, the two right panels) due to the resolution of the model and more challenging modelling conditions. At all sites, SWAN overestimates H_s in general. For site D the highest values for H_s is underestimated by SWAN, whereas for the fjord sites, site A and B, the highest occurring values are overestimated. The correlation for T_{m02} is not as good as for H_s (figure 6.5), and the quantile-quantile plot over-predict T_{m02}, except for the highest values, at all sites.

The resulting wave energy flux (E_f) from SWAN for the three sites correlates good enough with the flux calculated from buoy measurements (figure 6.6). SWAN at these locations underestimate E_f as a result of the correlation of H_s and T_{m02}. The calculation of E_f depends on T_{m02} and H_s, but as E_f is more sensitive to changes in H_s the correlation from T_{m02} does not have the greatest impact.

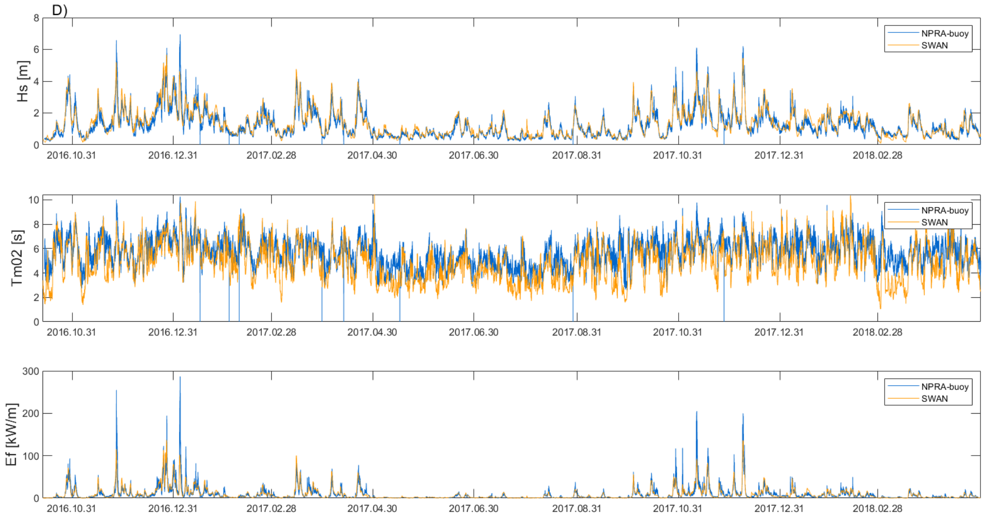

Figure 6.1: Comparison of waveparameters for NPRA buoys and SWAN at site D.

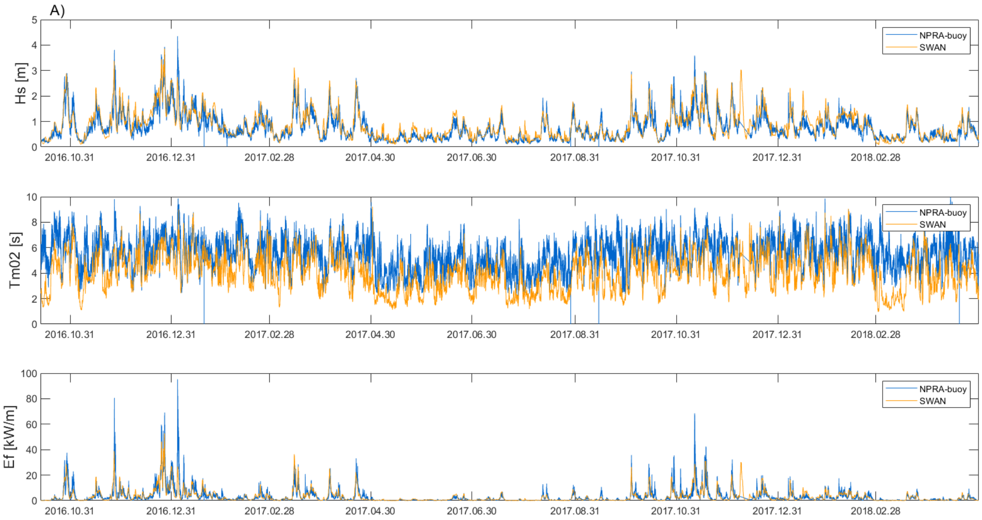

Figure 6.2: Comparison of waveparameters for NPRA buoys and SWAN at site A

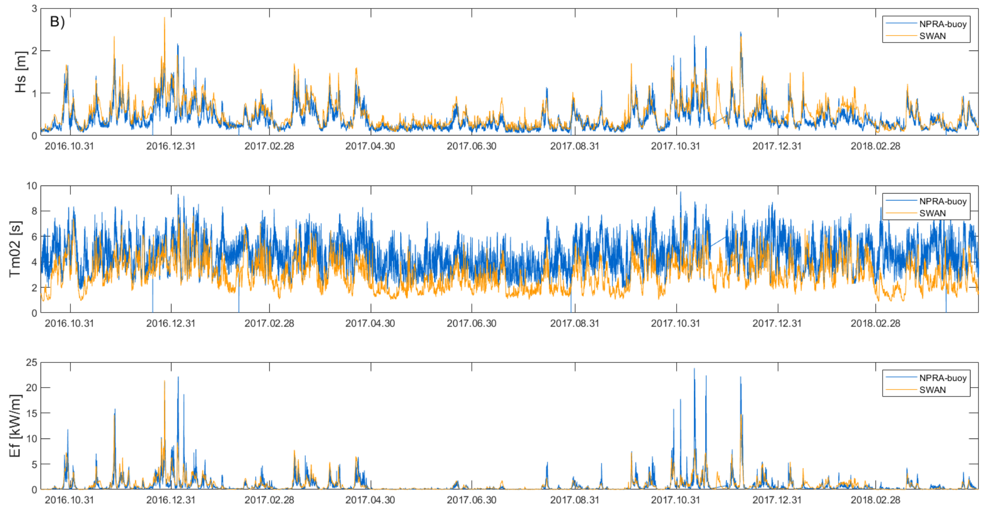

Figure 6.3: Comparison of waveparameters for NPRA buoys and SWAN at site B

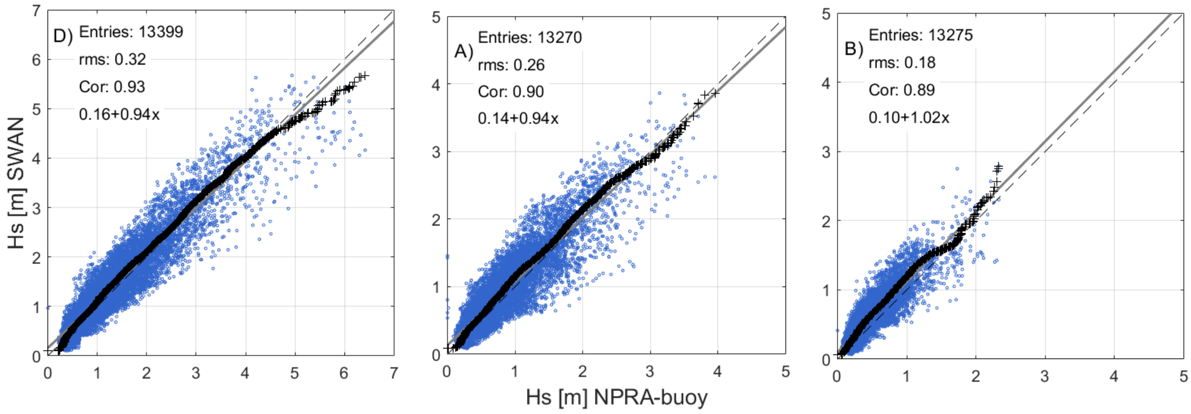

Figure 6.4: Scatter plots with corresponding regression lines and quantile-quantile plot of significant wave height H_s from NPRA buoys and SWAN, site D, A and B.

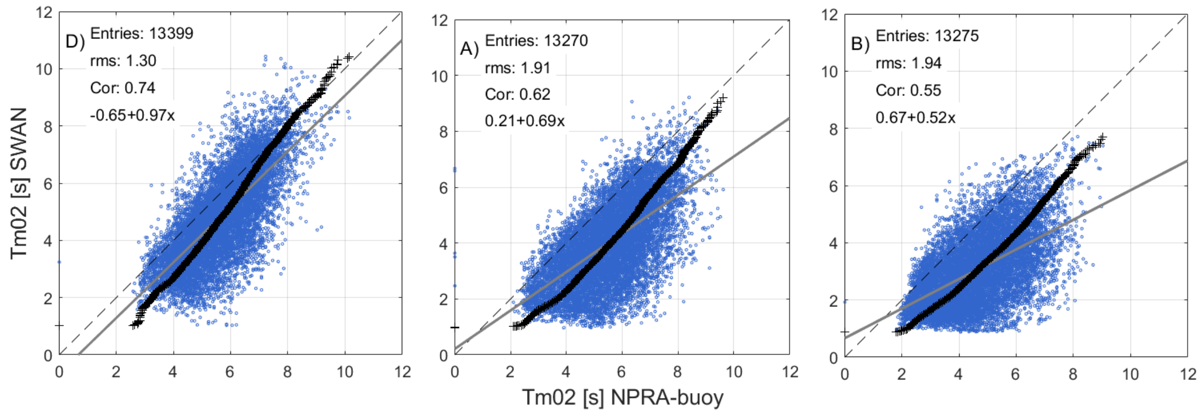

Figure 6.5: Scatter plots with corresponding regression lines and quantile-quantile plot of energy period T_{m02} from NPRA buoys and SWAN, site D, A and B.

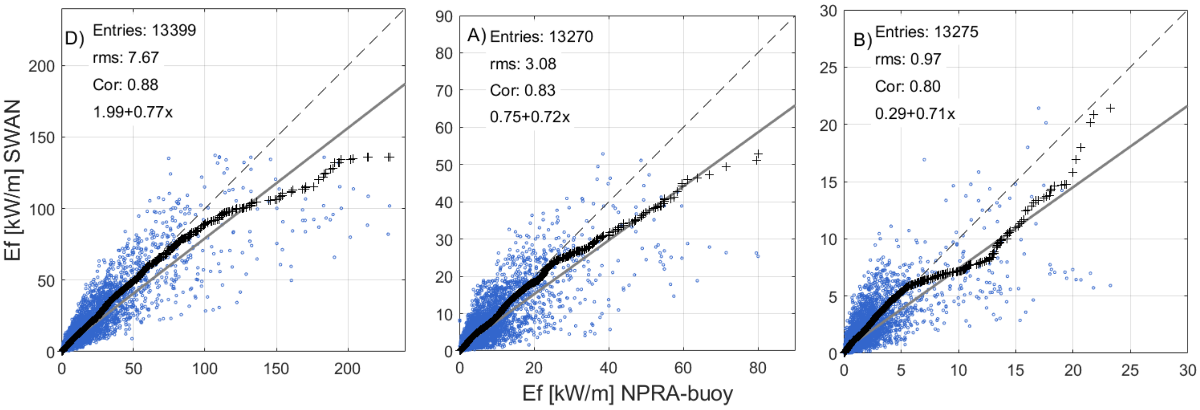

Figure 6.6: Scatter plots with corresponding regression lines and quantile-quantile plot of energy flux E_f from NPRA buoys and SWAN, site D, A and B.

6.2 Sulafjorden and Breisundet

6.2.1 SWAN 2007-2017

The result for SWAN from the period of 2007-2017 shows that H_s varies throughout each year at each site (A, B and D), but differs in magnitude for all three sites (figure 6.7). It is clear that point D experiences the highest values of H_s during the period. Further into the fjord, lower values of H_s are seen by comparing all panels in figure 6.7. Looking at the mean values it varies from 1.275 metres at site D to 0.472 metres at side B, furthest into the fjord (6.1). The 0.5 metres mean H_s line almost reaches site B (figure 6.8) indicating that energetic waves are commonly reaching far into the fjord. At site D the maximum H_s reaches 6.316 metres, whereas the largest value at site B reaches 2.964 metres (table 6.1). The maximum value seen at site B reaches far into the fjord and propagates into other arms of the fjord (figure 6.9). This result is expected as site D is more exposed to open ocean, and further into the fjord the positions are more sheltered and waves more exposed to refraction and diffraction.

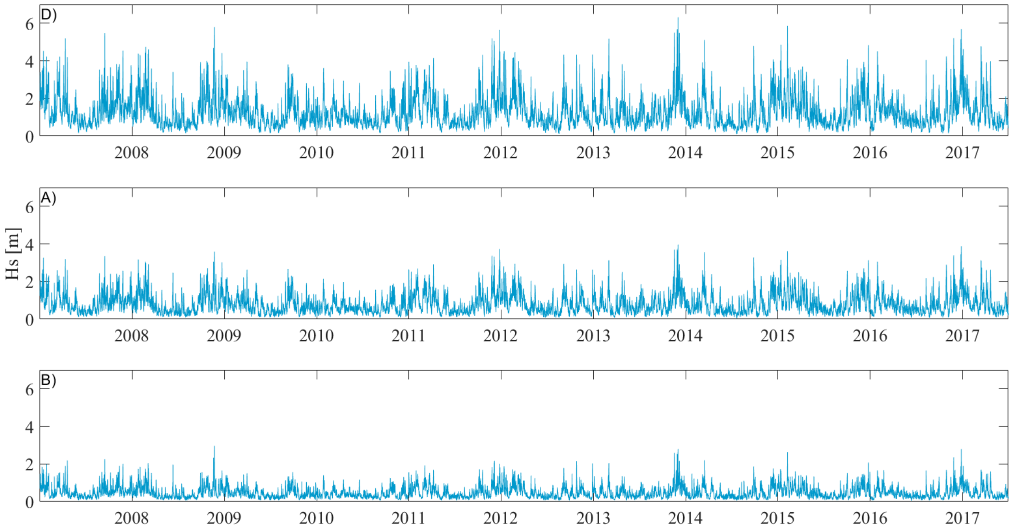

Figure 6.7: Significant wave height for position A, B and D in Sulafjorden and Breisundet from 2007 to 2017.

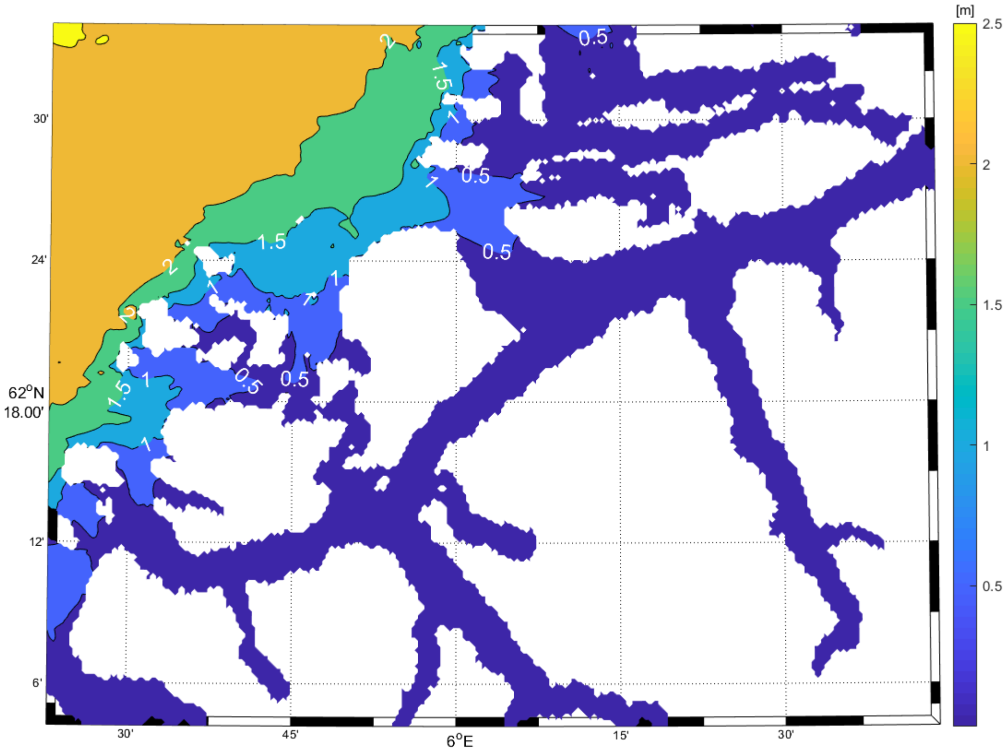

Figure 6.8: Mean H_s values from SWAN 2007-2017 at Sulafjorden and Breisundet.

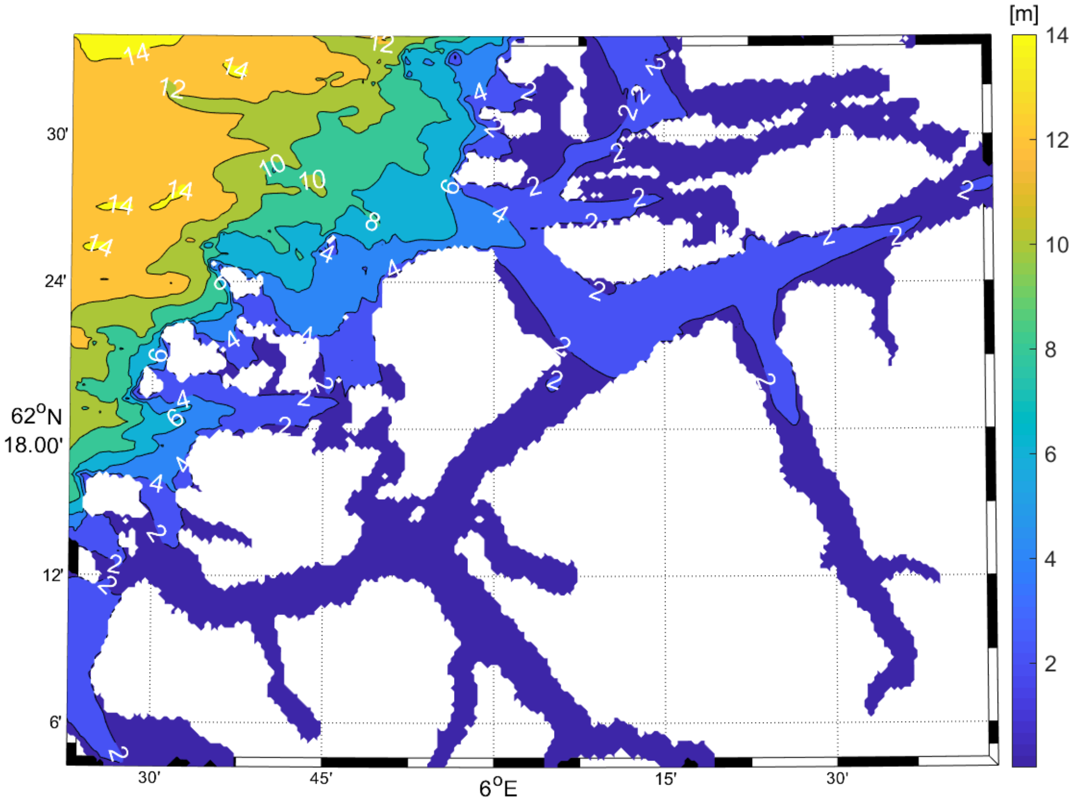

Figure 6.9: Max value of significant wave height for Sulafjorden and Breisundet from SWAN 2007-2017.

A strong seasonal variation appears at all sites for H_s (figure 6.7). The winter months are characterised by stronger H_s measures at all sites, and lower values during summertime. This is in accordance with what is expected from the characterising weather patterns at this latitude (recall the description of Sulafjorden and Breisundet in chapter 3.2). Wind speed is strongest at all times at site D and has a seasonal variation as well (figure 6.10). The same features are seen at all sites but the variation dampens further into the fjord. The wind direction at the different sites seems to be following the coastline in general but has components in all directions (figure 6.11). The wind speed and direction have some impact on the wave direction, but mainly the swell is dominating the wave direction. This is the reason for the difference seen in the rose plots for wind and wave direction (figure 6.11 and 6.12).

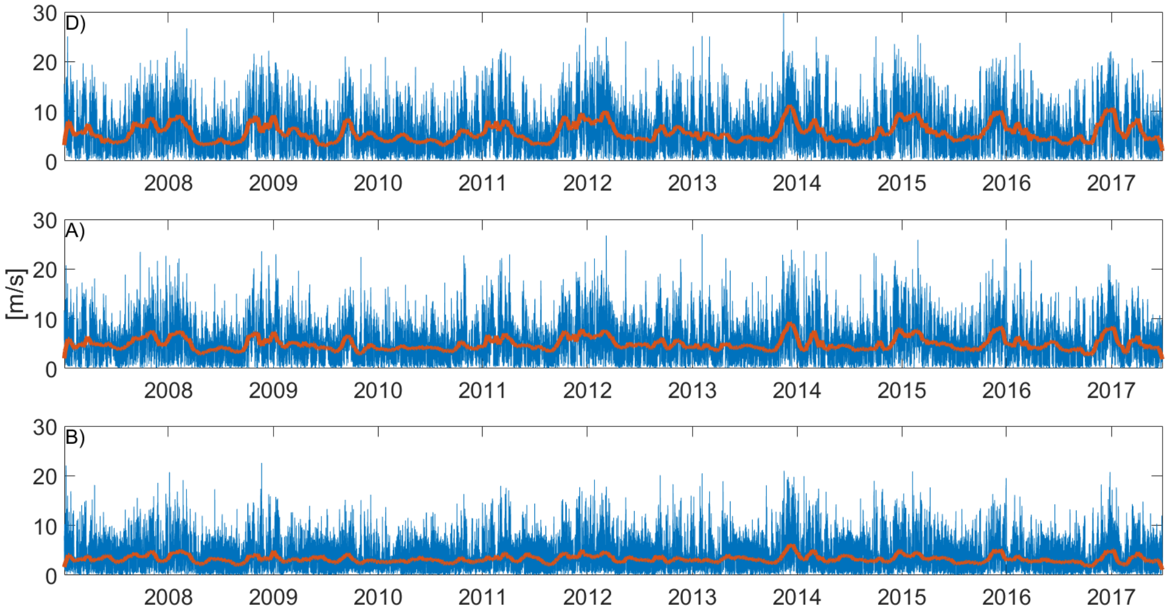

Figure 6.10: Wind speed variations for site D, A and B for SWAN from 2007-2017.

Looking at figure 6.12 the wave direction for the time-series corresponds to about 280-295°(coming from west-northwest), with not much variation. The corresponding mean wave direction is given in the rightmost panel in table 6.1, with 0°being North with increasing degrees clockwise. Data from the entire time-series shows that the wave direction varies more for site D than for site A and B (figure 6.12), again due to the offshore exposure at site D and sheltering effects further into the fjord for site A and B. Comparing the wind direction with the wave direction for site A and B, one would expect there to be a component with waves coming from south-southeast. This feature is not present. Swell dominates the mean wave direction.

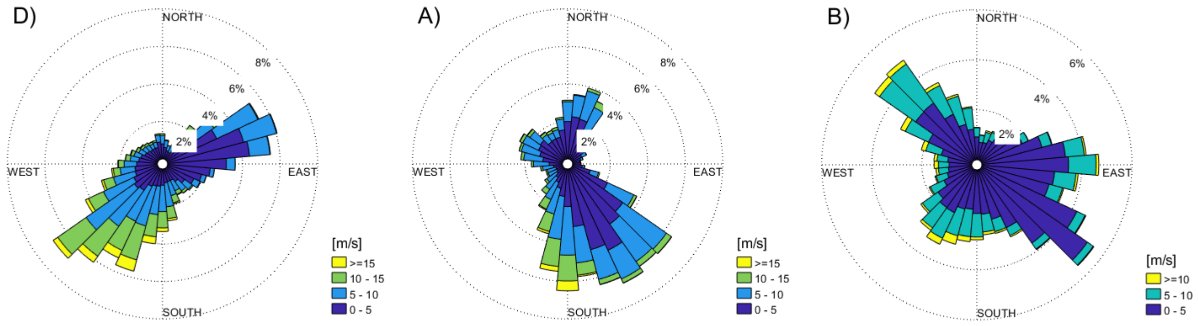

Figure 6.11: Wind direction with corresponding wind velocity values for site D, A and B for 2007-2017 from SWAN.

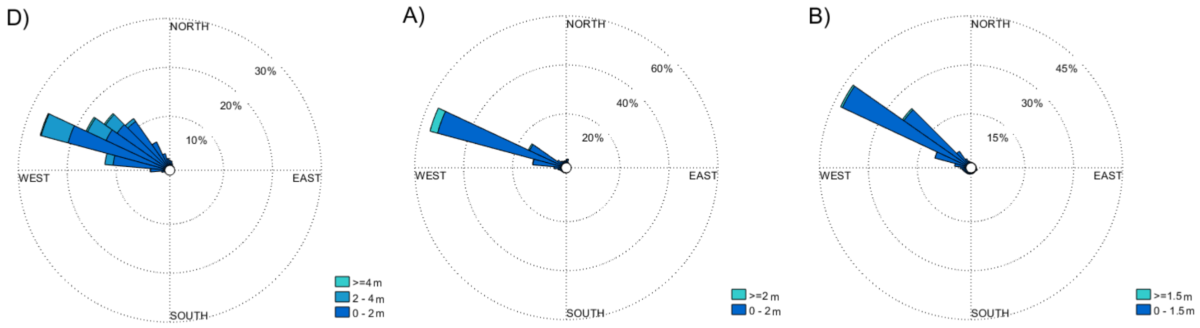

Figure 6.12: Wave direction with corresponding H_s values for site D, A and B for 2007-2017 from SWAN.

SITE	**MEAN H_s [m]**	**MAX H_s [m]**	**MEAN WAVE DIR. [deg]**
Site A	0.805	3.962	282.5
Site B	0.472	2.964	290.3
Site D	1.275	6.316	295.0

Table 6.1: Statistical measures for site A, B and D from SWAN 2007-2017. The direction is referring to where the waves are coming from.

The mean peak period map is showing features which indicates that the impact of swell on this area is significant (figure 6.13). A mean peak period of over 9 seconds reaches past site B. This value would not be possible to see if not for the swell coming from the open ocean. Offshore the mean peak period is above 10s. This signature continues into the fjord.

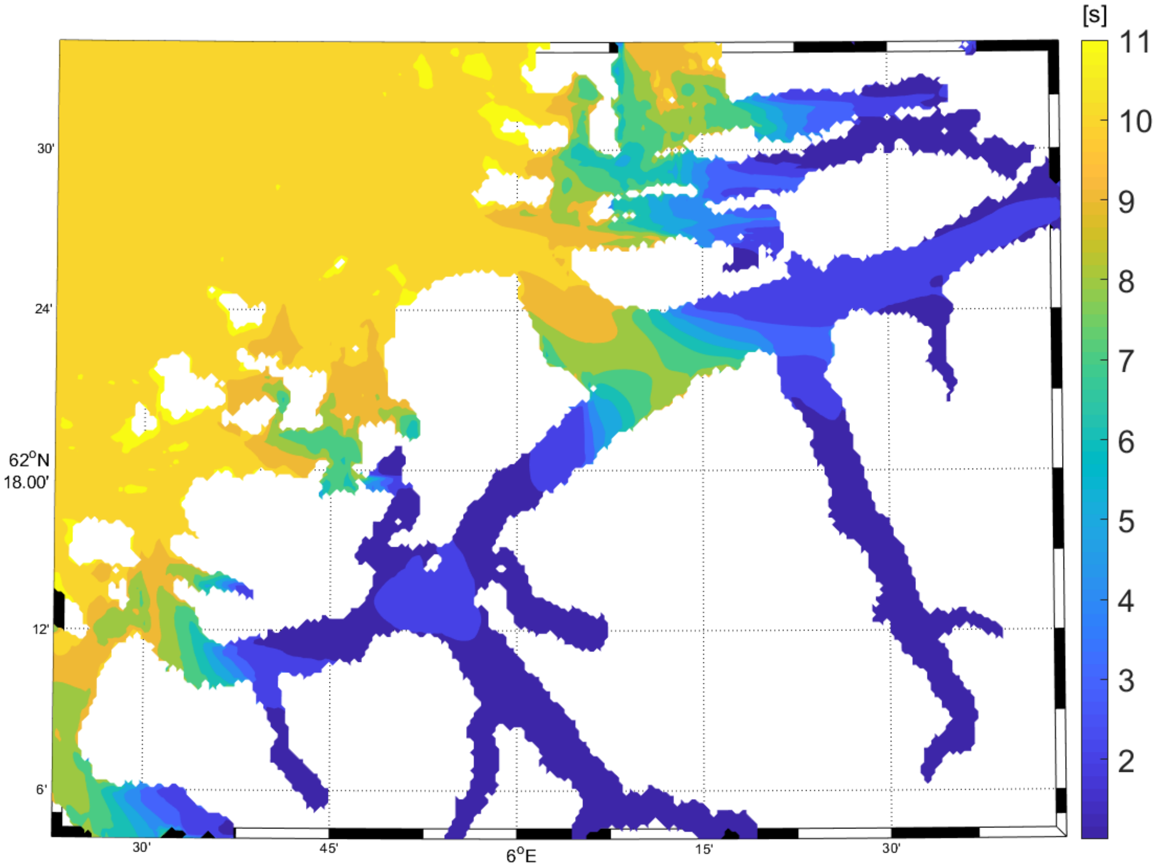

Figure 6.13: T_p (Mean peak period) for SWAN 2007-2017.

6.2.2 NPRA buoys October 2016 - December 2018

Buoy data for site A, B and D show the same variation as for SWAN regarding the wave climate, despite the difference in the measurement period. D has the highest occurring H_s, and site B the lowest occurring H_s (figure 6.14). The seasonal changes are apparent from the buoys as well, with distinctive differences between summer and winter. Looking at the wind direction (figure 6.15) the topography leads the wind as SWAN indicated. The wind distribution seen at site A and B is different from site D. Both site A and B experience mostly winds from the south. Site B also experience wind coming from south-east and north-west. The wave directions are in accordance with SWAN directions (figure 6.16) with dominating direction from west-northwest. Table 6.2 gives the mean and max H_s, and the mean wave direction from the buoy data for 2016-2018. Comparing this to the table for SWAN (table 6.1) some variation is seen, but not worth considering as expected from the validation in chapter 4.3. These values are also for different periods of time and averaged over different length (2007-2017 for SWAN versus 2016-2018 for NPRA buoys).

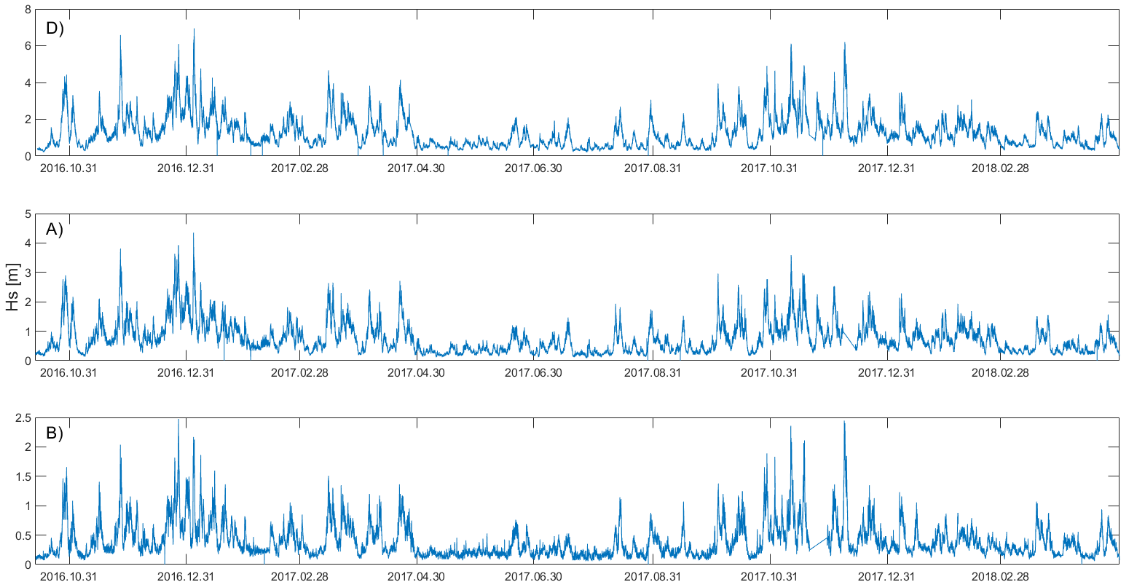

Figure 6.14: Significant wave height for position A, B and D in Sulafjorden and Breisundet from buoy measurements 2016-2018.

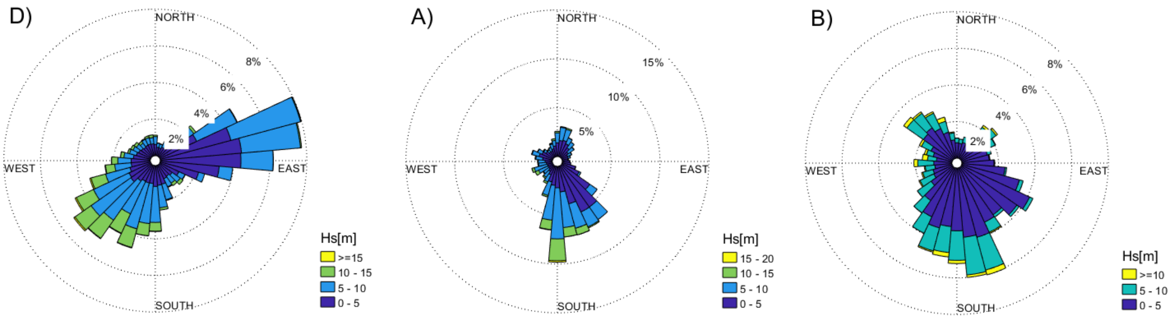

Figure 6.15: Wind direction with corresponding wind velocity values for site D, A and B for 2016-2018 from the NPRA buoys at 4m height.

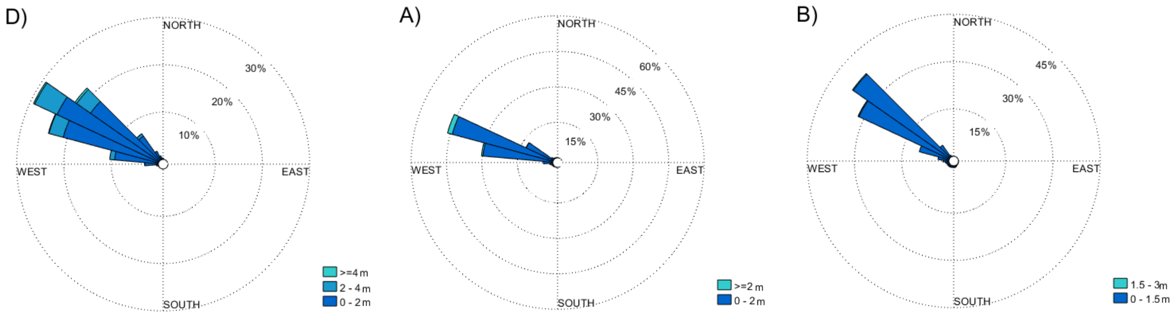

Figure 6.16: Wave direction with corresponding H_s values for site D, A and B for 2016-2018 from the NPRA buoys.

SITE	MEAN H_s [m]	MAX H_s [m]	MEAN WAVE DIR. [deg]
Site A	0.752	4.350	285.9
Site B	0.384	2.476	293.3
Site D	1.223	6.943	298.2

Table 6.2: Statistical measures for site A, B and D for NPRA buoys. Mean direction is given in degrees from.

6.2.3 Winter-trend from SWAN for 2007-2017

The trend for H_s for site D, for the winter months (December, January and February) is shown in figure 6.17. The figure shows the mean values for each month, and a slightly positive trend is found. None of the winter months stands out as dominating with high values of H_s, as for each winter it varies. The trend starts at 1.5 metres and changes to about 1.75 metres in the end of the time-series, resulting in a positive trend of about 0.25 metres.

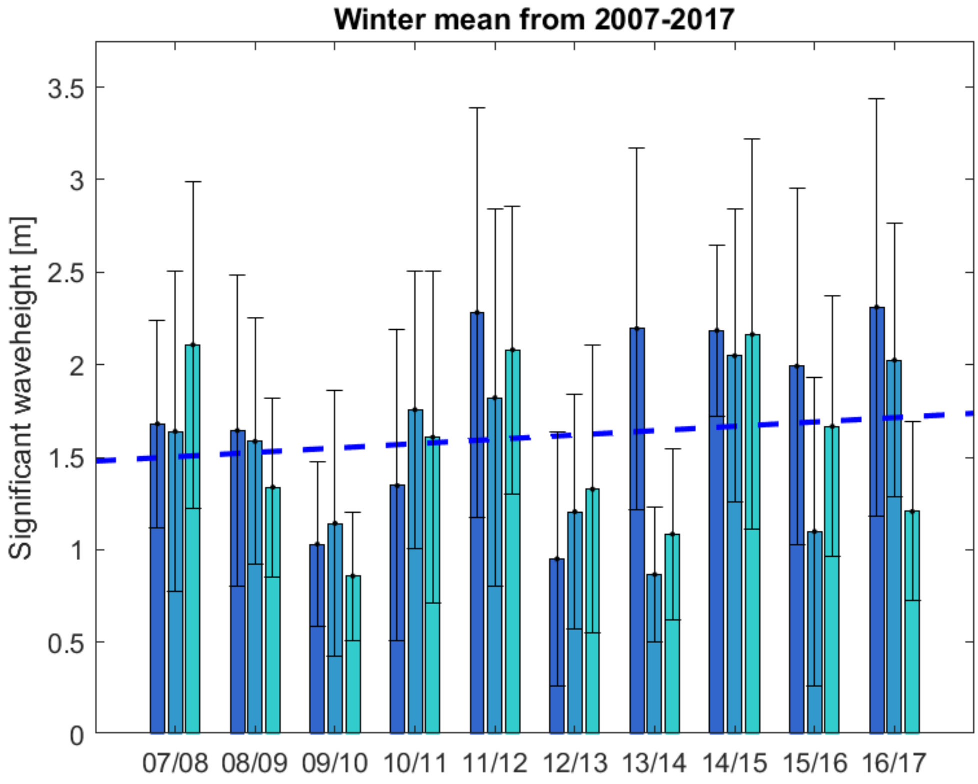

Figure 6.17: Mean H_s values for the winter months for site D. The three grouped bars corresponds to December, January and February, with errorbar corresponding to the standard deviation. The dashed blue line is the fitted trendline.

6.3 Case study 24-28. December 2017

Comparing offshore points to the most inner points in the fjord from the case study from SWAN for December 2017, the reduction in H_s is clear (figure 6.18). The outermost points experience the highest waves and the points furthest into the fjord experience the lowest waves. All sites show the same tendency throughout the series, whereas the trend is damped at site 9, 10 and 11. H_s has the highest value midway through the 26th of December, reaching almost 4 metres. All data from this SWAN run is included for H_s in figure 6.18, even the startup values, as seen for the first 3 hours. These first measurements show that the model is starting to calculate.

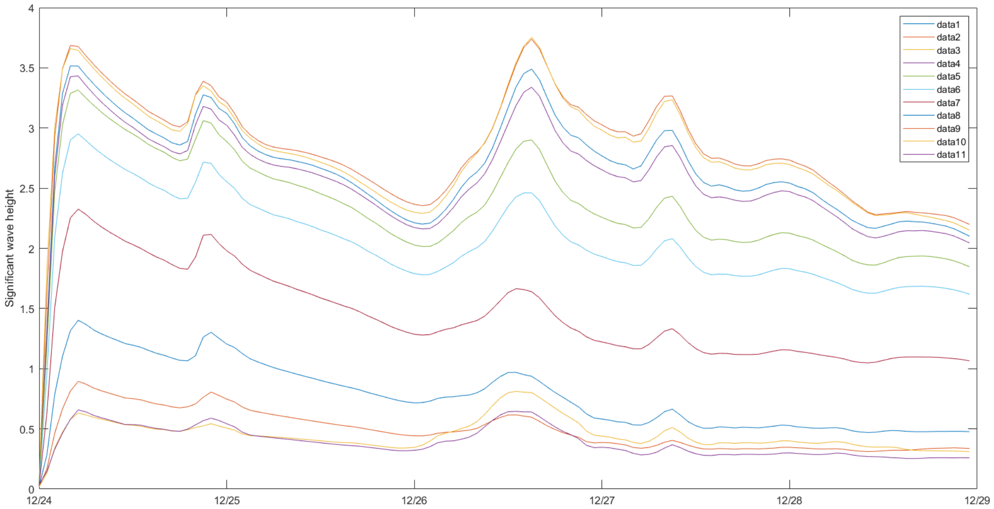

Figure 6.18: Significant wave height for all sites from the case study for December 2017. The different coloured lines represent the different sites from figure 4.2.

Comparing T_{m-10} and T_{m02} different values are found (figure 6.19 and 6.20). For all sites the tendency for all T_{m-10} and T_{m02} is similar but differs in magnitude. The outermost points have the highest values, and opposite for the points furthest into the fjord. The difference in magnitude stays approximately the same during the run, except for the 25th and 26th December. Here the difference for T_{m02} values between all sites decrease to 2 seconds and 1 second for T_{m-10}. The same is seen for T_{m-10} at the end of the 28th of December. This change in magnitude difference is not seen in the H_s values for the same period.

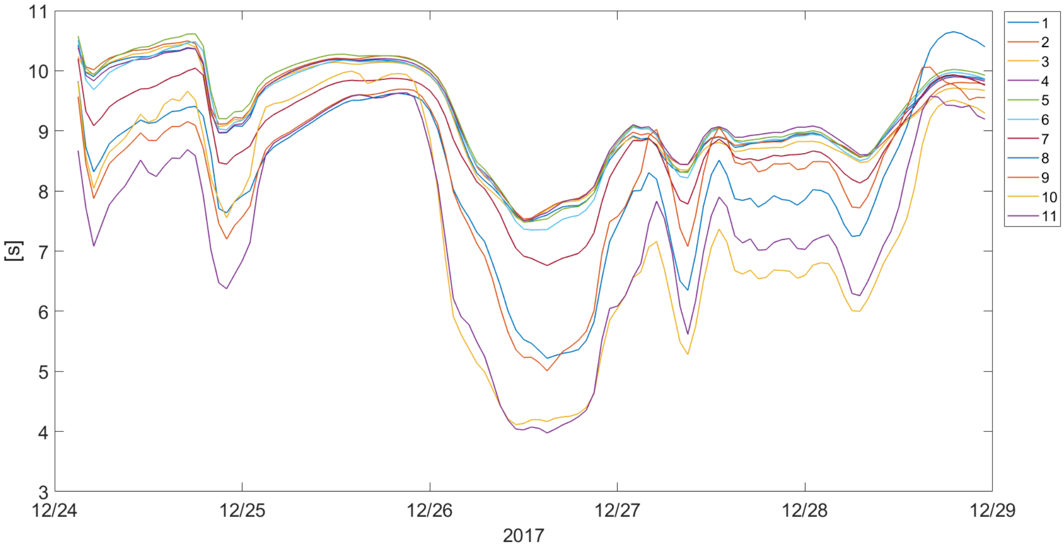

Figure 6.19: T_{m-10} evolution for all sites from the case study for December 2017.

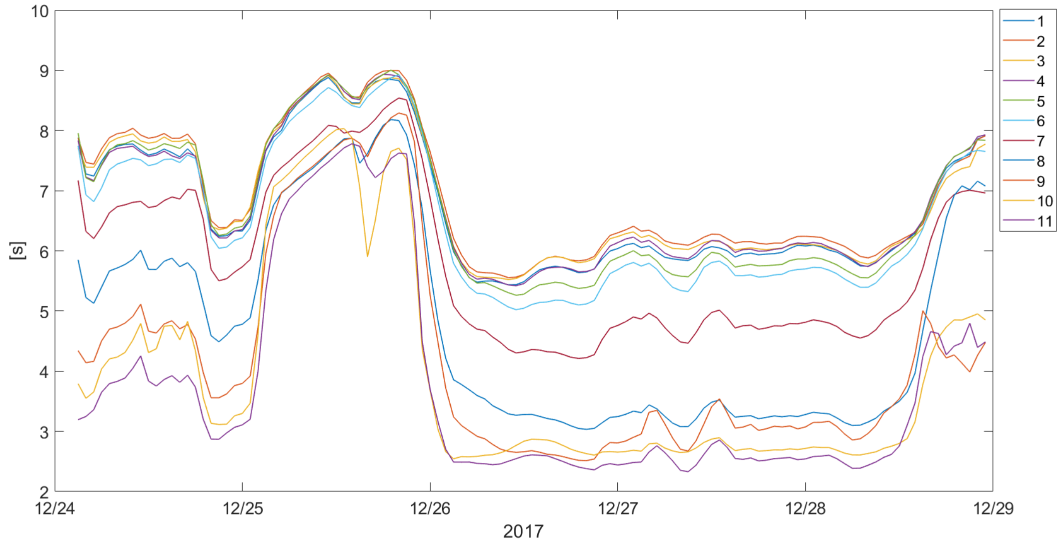

Figure 6.20: T_{m02} evolution for all sites from the case study for December 2017.

Comparing mean T_p for each day in figure 6.21 for panel b (corresponding to the mean T_p for the 25th of December), it is seen that T_p is equal for all sites. This explains the mentioned feature from the wave period plots (25th of December from figure 6.19 and 6.20), indicating that swell is dominating the whole area during this day. A value of about 12 seconds is found.

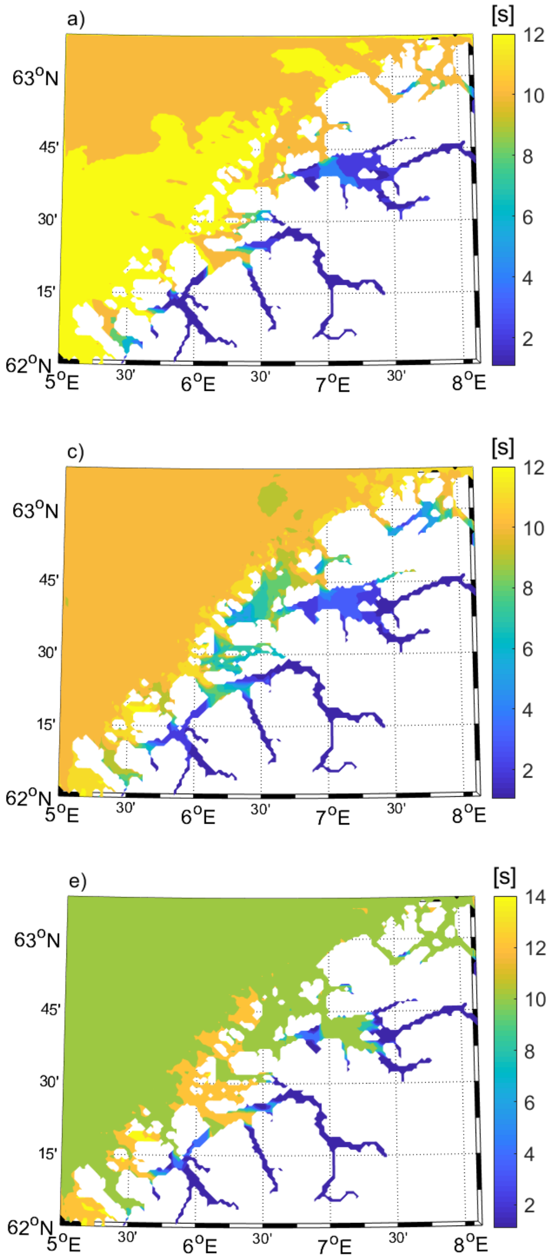

Figure 6.21: Mean T_p for each day of the case study for December 2017. a)=24.12, b)=25.12, c)=26.12, d)=27.12, e)=28.12.

6.4 Energy Period Investigations

In the search of the most correct α value, the case study from Christmas 2017 is included. Figure 6.19 and 6.20 is plotted together for site D and B for comparison in figure 6.22. T_{m-10} is in general longer than T_{m02}, but both show the same trends over time. The difference at all sites is smaller for T_{m-10} than for T_{m02}. To retrieve the most correct α

value two cases are included, one where α is a constant value calculated from the mean α from site D, A and B and one with different α specifically calculated for each site.

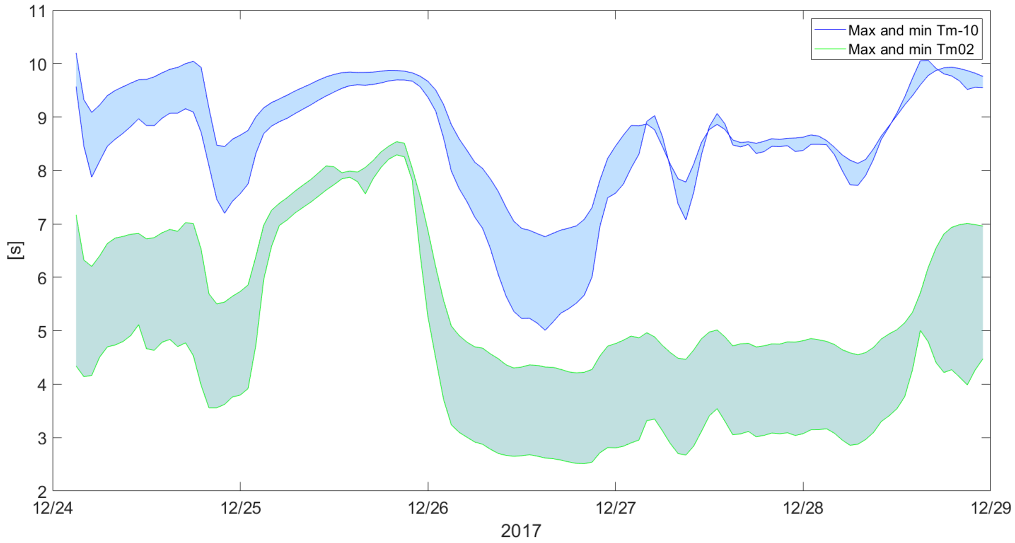

Figure 6.22: T_{m02} and T_{m-10} evolution for all site D and B from the case study for December 2017 (where max refers to site D and min refers to site B).

Alpha values for SWAN December 2017:

- Site D: α=1.5.
- Site B: α=1.9
- Mean α=1.7

The first two α values are related to the second case mentioned above, and the mean α value to the first case with a constant α.

In case one the energy period is over and underestimated for site D and B by the use of constant α value (figure 6.23). But, the shape is preserved and the values are more equal than with T_{m02} without any α. The largest deviation is seen for the 25th of December.

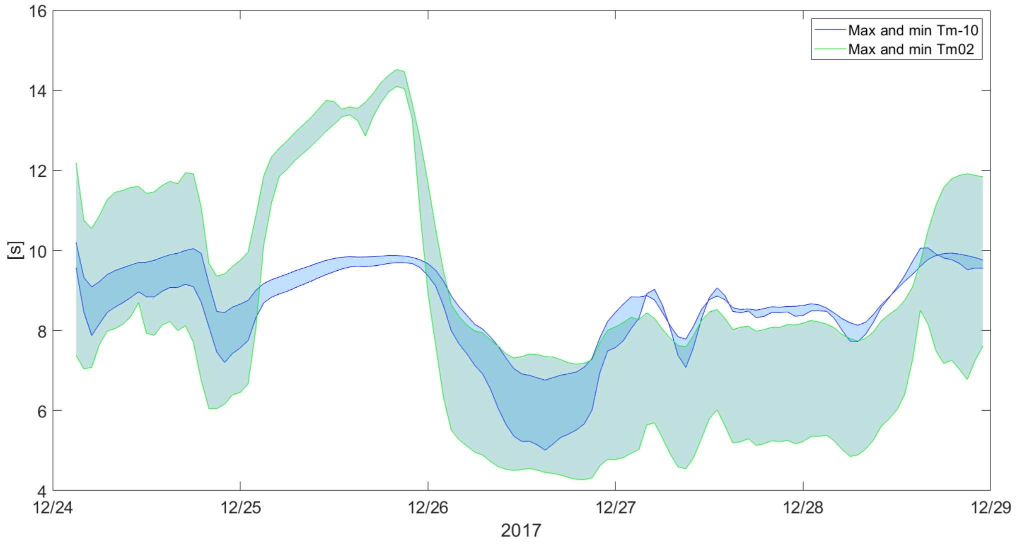

Figure 6.23: T_{m02} and T_{m-10} evolution site D and B with constant α=1.7 from the case study for December 2017.

By using α=1.5 for site D and α=1.9 for site B, the second case, the wave period T_{m02} shows similar magnitude and shape as the energy period T_{m-10} (figure 6.24). The values are more similar to T_{m-10} than the result from the constant α value. Still, the result is not 100 % accurate, and the deviation for December 25th is present in this case as well.

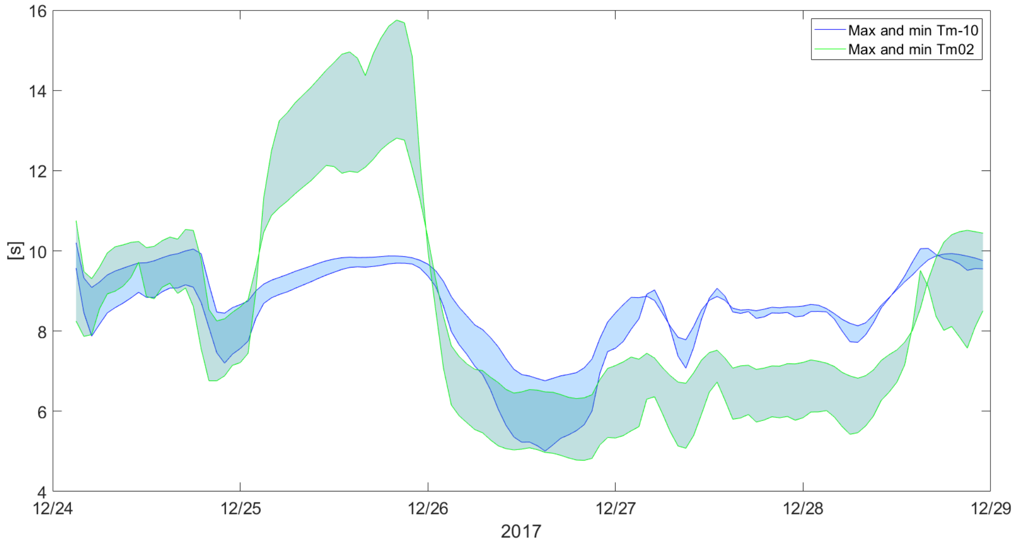

Figure 6.24: T_{m02} and T_{m-10} evolution for all sites with α=1.5 for site D and α=1.9 for site B, from the case study for December 2017.

Considering the SWAN period from 2007-2017 the evolution of WPR shows a seasonal change. Winter months have in general higher values of WPR than summer months, as seen from figure 6.25. This seasonality provides issues when estimating alpha values as the ratio between T_{m-10} and T_{m02} differs.

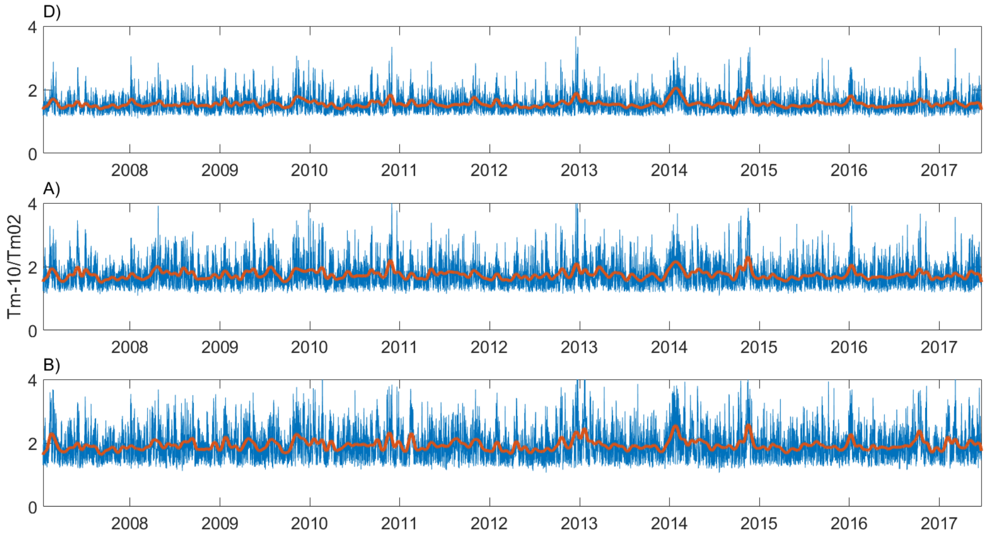

Figure 6.25: WPR evolution for sites D, A and B for SWAN 2007-2017.

The use of the different energy wave periods affects the calculated energy flux, as seen in figure 6.26 (The E_f lines with no α correspond to E_f calculated with Tm_{-10}). For site D both cases of α values lead to overestimating the energy flux almost at all times. The site specified value gives the most correct result. The difference is either way not resulting in a great difference from the energy flux calculated with Tm_{-10}. For site B the energy flux is lower than 5 kW/m during the whole time-series, and the two cases of different α values do not have significant impact.

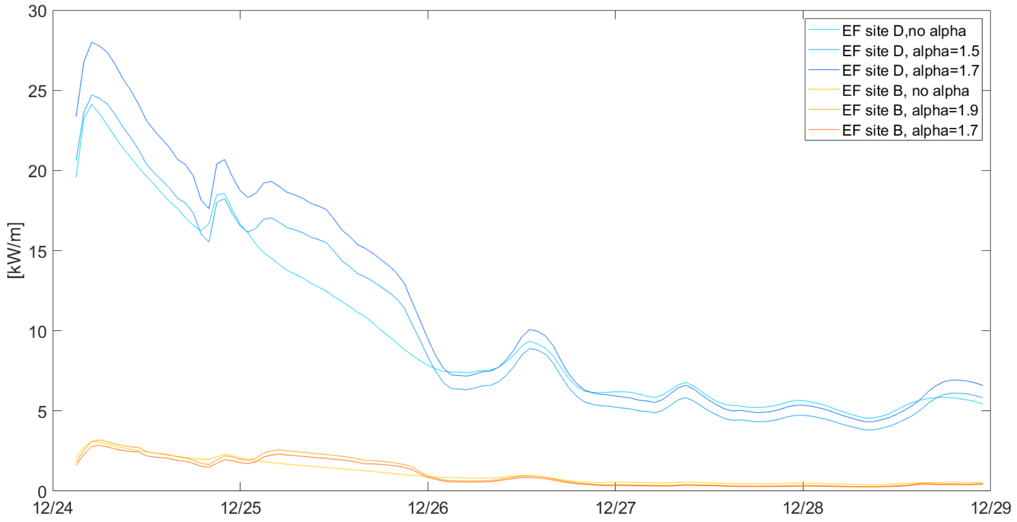

Figure 6.26: Energy flux for site D (blue) and B(yellow) for December 2017. E_f calculated with T_{m-10} corresponds to the line with no alpha.

The two cases of different α values are applied on the SWAN series from 2007-2017 for comparison for site D and B (figure 6.27). Both cases overestimate the energy flux at both sites, with the greatest impact on site D.

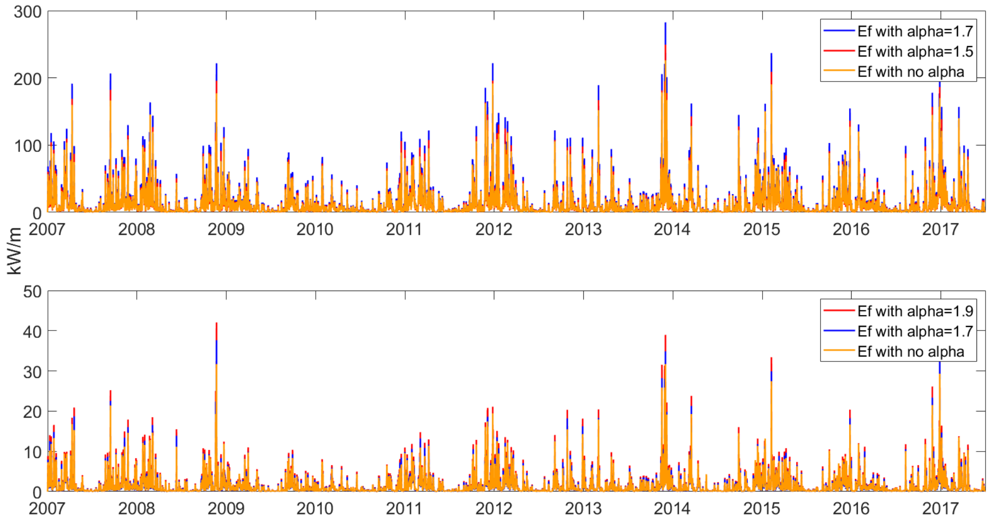

Figure 6.27: Energy flux for site D (upper panel) and B(lower panel) for SWAN 2007-2017 calculated with different alpha values compared to Tm-10.

Overlapping E_f from SWAN spectrum data and E_f from NPRA buoys calculated with T_{m02} and specified alpha values for each location are compared in figure 6.28. E_f

from NPRA buoy calculations gives in general higher values than for E_f from SWAN. The different panels have different magnitude on the y-axis, from this it is seen that the difference for E_f for the two data sets is higher for site D.

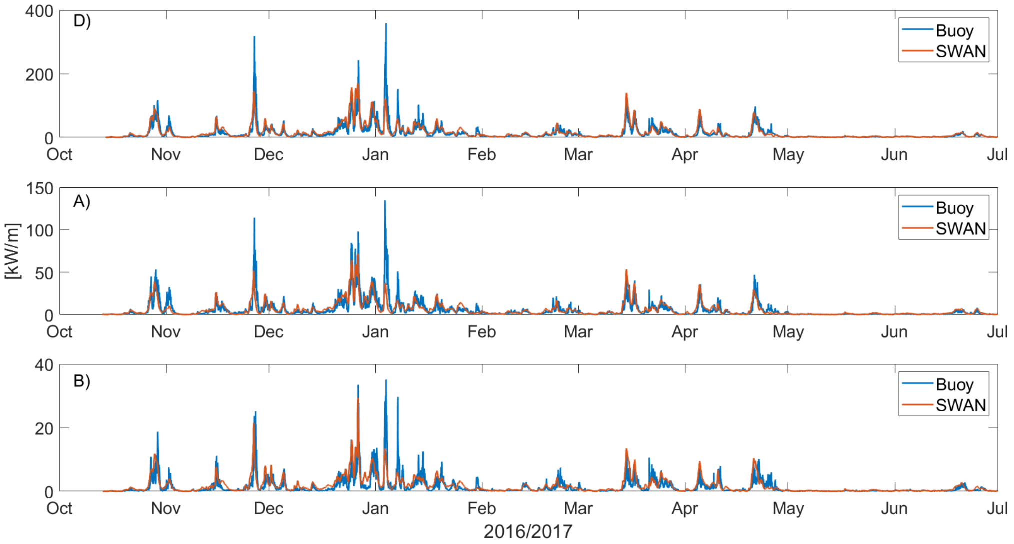

Figure 6.28: Energy flux for site D, A and B for NPRA buoys and SWAN for October 2016 to July 2017.

6.5 Wave Energy Flux in Sulafjorden and Surrounding Area

Combined scatter and energy diagrams give the calculated wave energy flux E_f for Sulafjorden in figure 6.29. From these energy scatter diagrams the wave climate is again described. The isolines represent lines with constant energy flux values. Colours indicate the occurrence of each value per year, with numbers representing the sum of the energy flux for each H_s and T_e per year. The highest amount of the wave energy is found at site D, in accordance with the values for H_s from figure 6.7. For site D (top panel in fig. 6.29), the highest density of repeating energy flux for the time-series 2007-2017 corresponds to energy period of about 7-11 seconds and H_s of 1-4 metres. This relates to an E_f interval 5-70 kW/m, indicating a large variation. The E_f distribution per year is spread out extending from values close to zero to over 200 kW/m.

At site A the highest density of energy is found at about the same energy period as for site D, but H_s is reduced to 0.5-2.5 metres. The wave EF interval is more narrow than for site D, here it varies from about 1 kW/m to 30 kW/m with the highest occurring value is almost 100 kW/m. Energy period of 6-10 seconds and H_s of 0.5-1.5 metres indicates the area of highest energy density at site B (figure 6.29). The narrowest interval of E_f values is found at site B where the highest value almost reaches 50 kW/m. Averaging the energy flux at site D, A and B (table 6.3), the result is as expected. Site D has the highest mean value of 10.6 kW/m, and B has the lowest with 1.2 kW/m. The same is seen for the maximum energy flux occurring for the period, D has the highest and B has the lowest value.

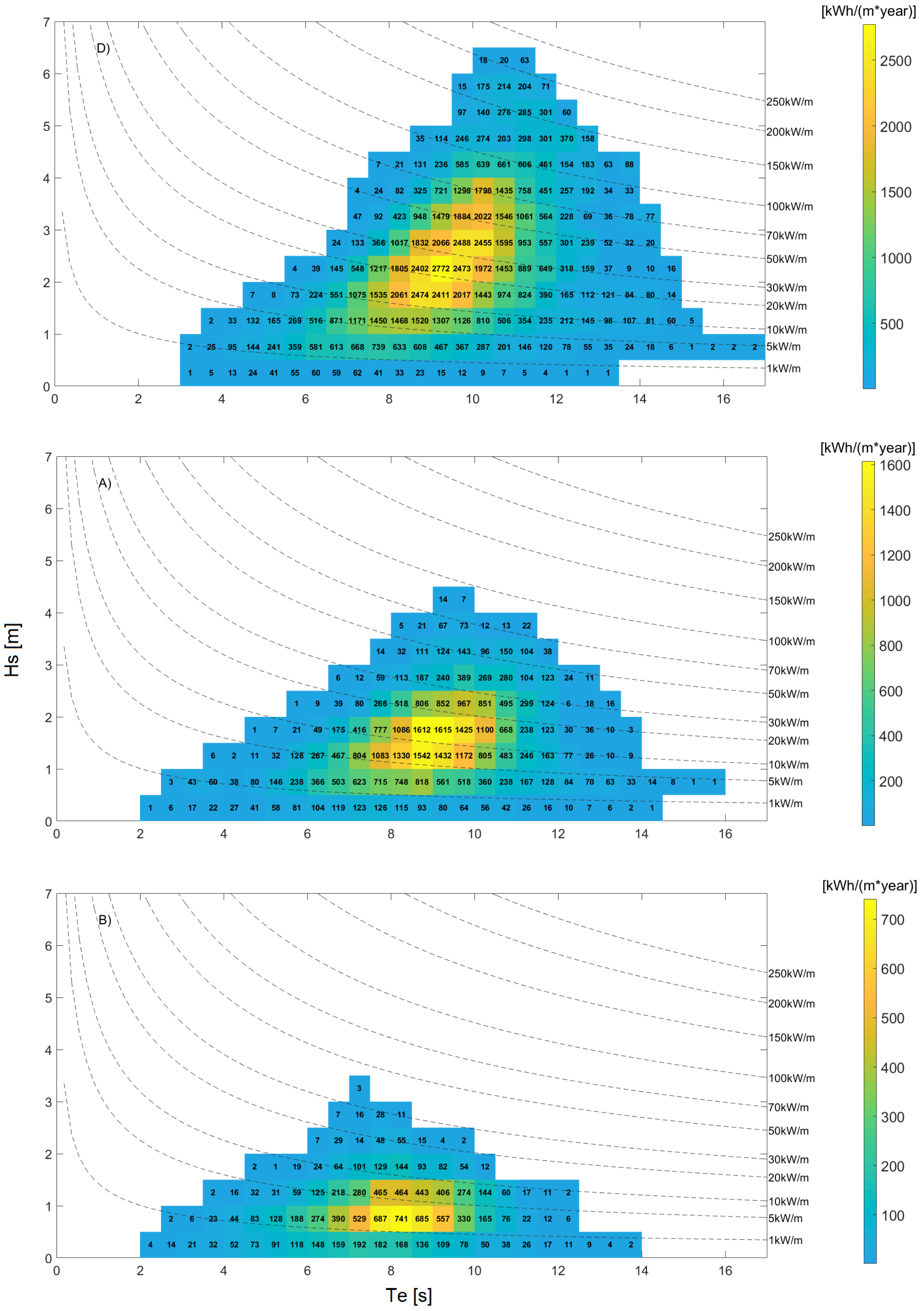

Figure 6.29: Wave energy flux in [kWh/(m*year)] for site D, A and B from SWAN 2007 to 2017. Dashed lines presenting lines of constant energy flux. Colours with numbers show the contribution of E_f to the total energy flux.

Site	Coordinates	Depth[m]	E_f Mean [kW/m]	E_f max [kW/m]
D	62.4405N 5.9349E	345	10.6	226.0
A	62.4275N 6.0452E	370	4.1	78.5
B	62.4026N 6.0802E	334	1.2	31.7

Table 6.3: Position, depth, Mean E_f and Max E_f for site D, A and B.

From Fig. 6.30, it is clear how much the wave energy reduces as the waves reach inshore, and how large the potential is out in the open ocean. The fjord sites represent in general smaller amounts of mean wave energy flux compared to offshore sites but have a more constant supply. It is seen that the flux weakens less when entering the fjord, and a large amount of energy reaches Breisundet before it dampens to values represented by the other nearby fjords.

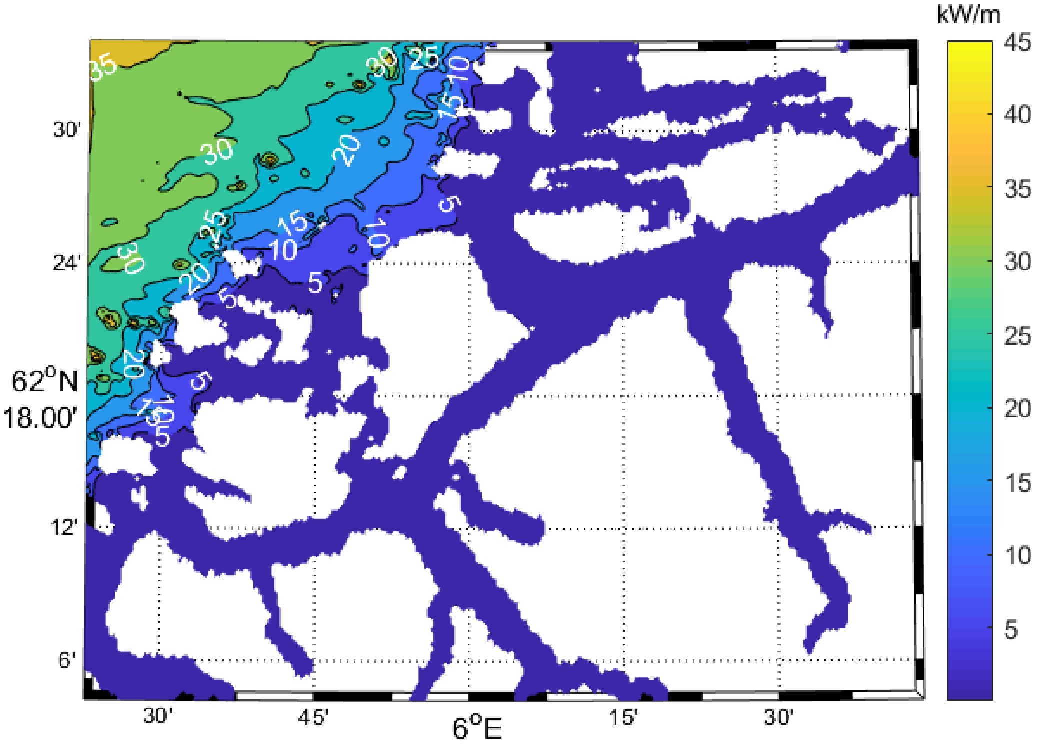

Figure 6.30: Mean wave energy flux for SWAN 2007-2017.

From the seasonal trend appearing from H_s (figure 6.7) it is expected to see the same trend in the energy flux. Figure 6.31 shows statistical values for each month from site

D. Each box consists of the median (the central mark), and the top and bottom edges indicate the 75th and 25th percentiles. The whiskers represent the most extreme data points, without outliers. The '+' symbol marks outliers. The seasonality corresponds well to the expected trend with higher values during winter and autumn and lower values for summer and spring months. At site A and B the wave energy flux is more constant, but still show seasonal variation (figure 6.32). Furthest into the fjord, at site B, the least amount of available energy flux appears, but also the most constant values sizewise occurs. The wave conditions at this position are more stable throughout the year, due to being more sheltered.

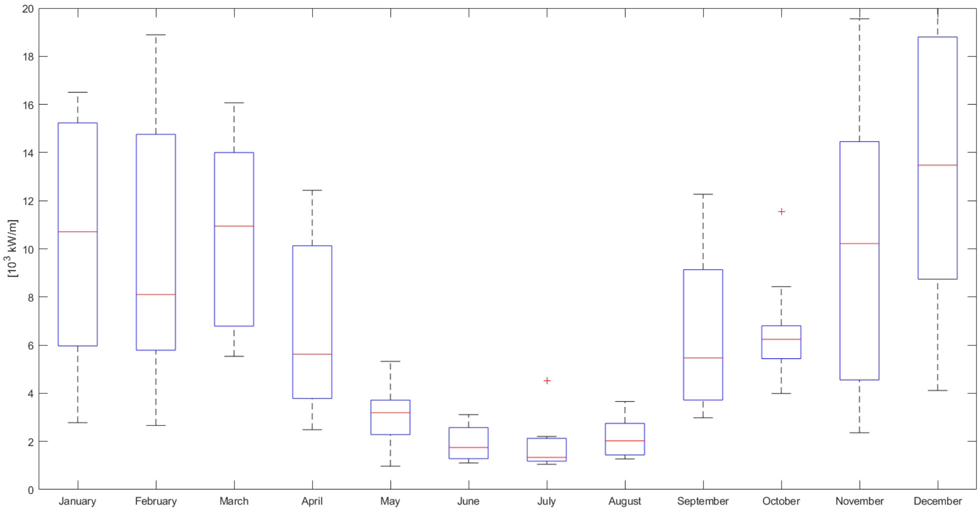

Figure 6.31: Mean wave energy flux box plot for each month at site D from SWAN for 2007-2017.

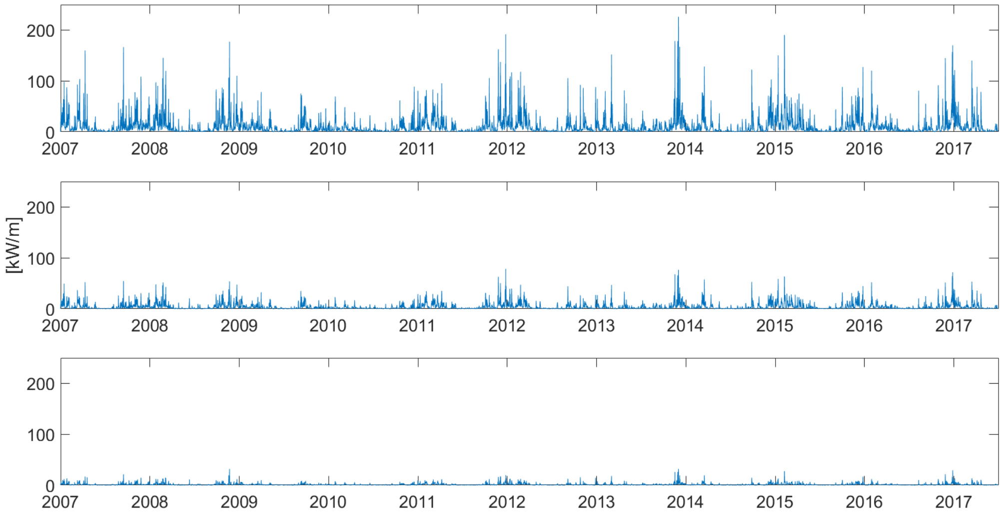

Figure 6.32: Wave energy flux variations for site D, A, and B.

Seasonal scatter wave energy plots for site D, A and B are included to further investigate the seasonal change in E_f (DJF=December, January and February, MAM=March, April, May, JJA=June, July and August, SON=September, October, November). At site D the seasonal change in wave energy flux is distinctive (figure 6.33). For site A and B a seasonal change is also featured, but a more constant supply throughout all months is found (figure 6.34 and 6.35). June, July and August have the lowest values for all sites. The most energetic intervals for H_s and T_e are similar for autumn, winter and spring whereas summer has significant lower values of H_s contributing to the highest density of energy.

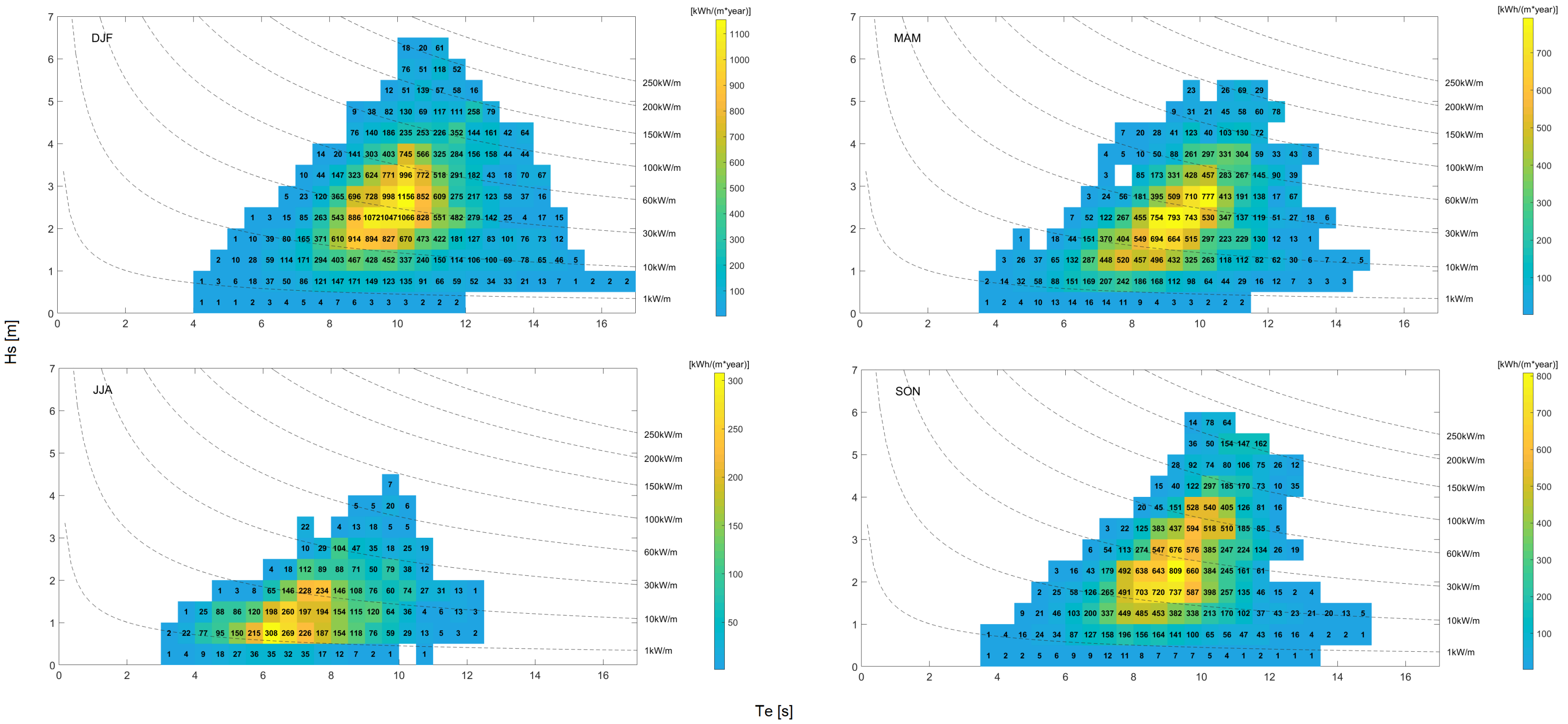

Figure 6.33: E_f in [kWh/(m*year)] for the different seasons at site D from SWAN 2007-2017. Dashed lines presenting lines of constant energy flux. Colours with numbers show the contribution of E_f to the total energy flux.

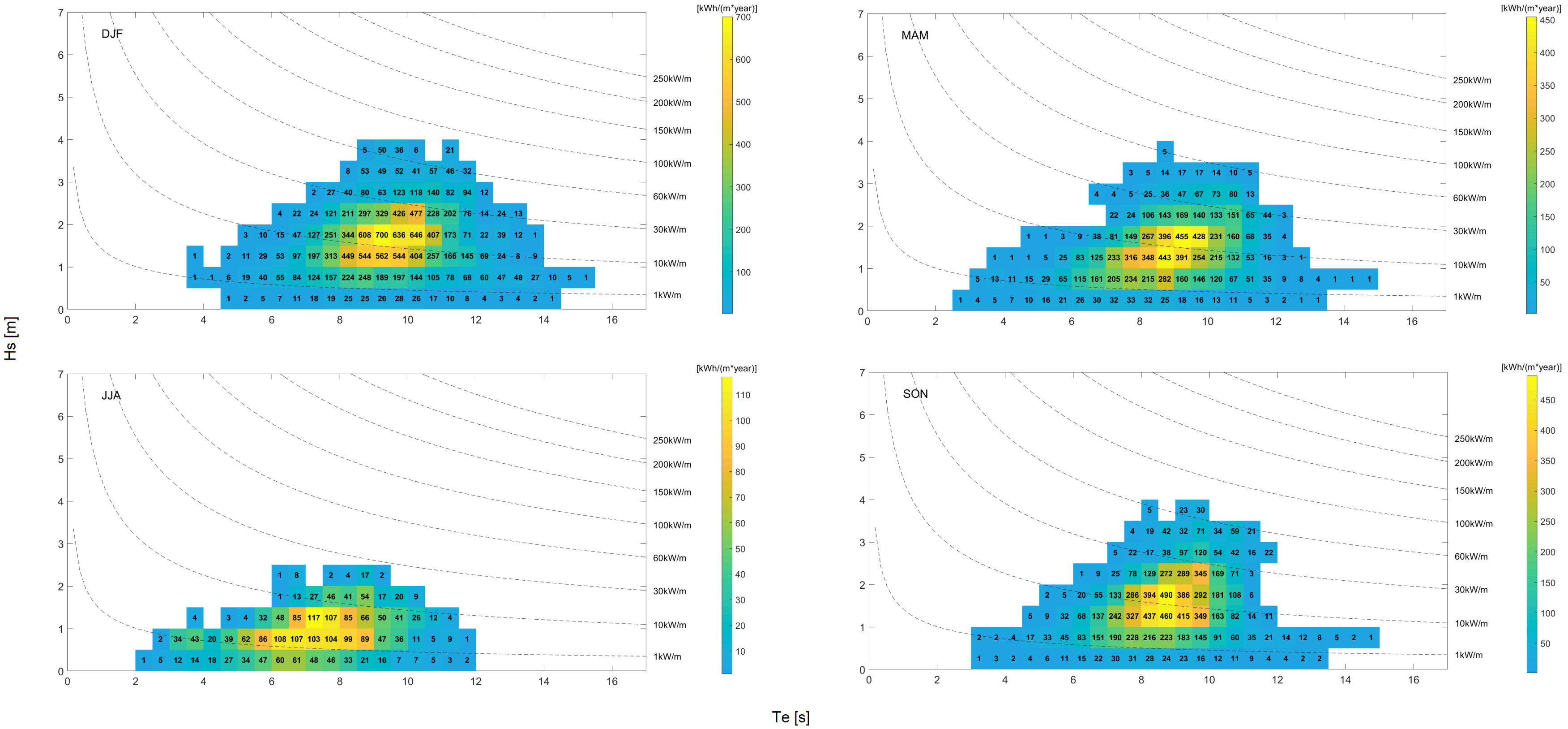

Figure 6.34: E_f in [kWh/(m*year)] for the different seasons at site A from SWAN 2007-2017. Dashed lines presenting lines of constant energy flux. Colours with numbers show the contribution of E_f to the total energy flux.

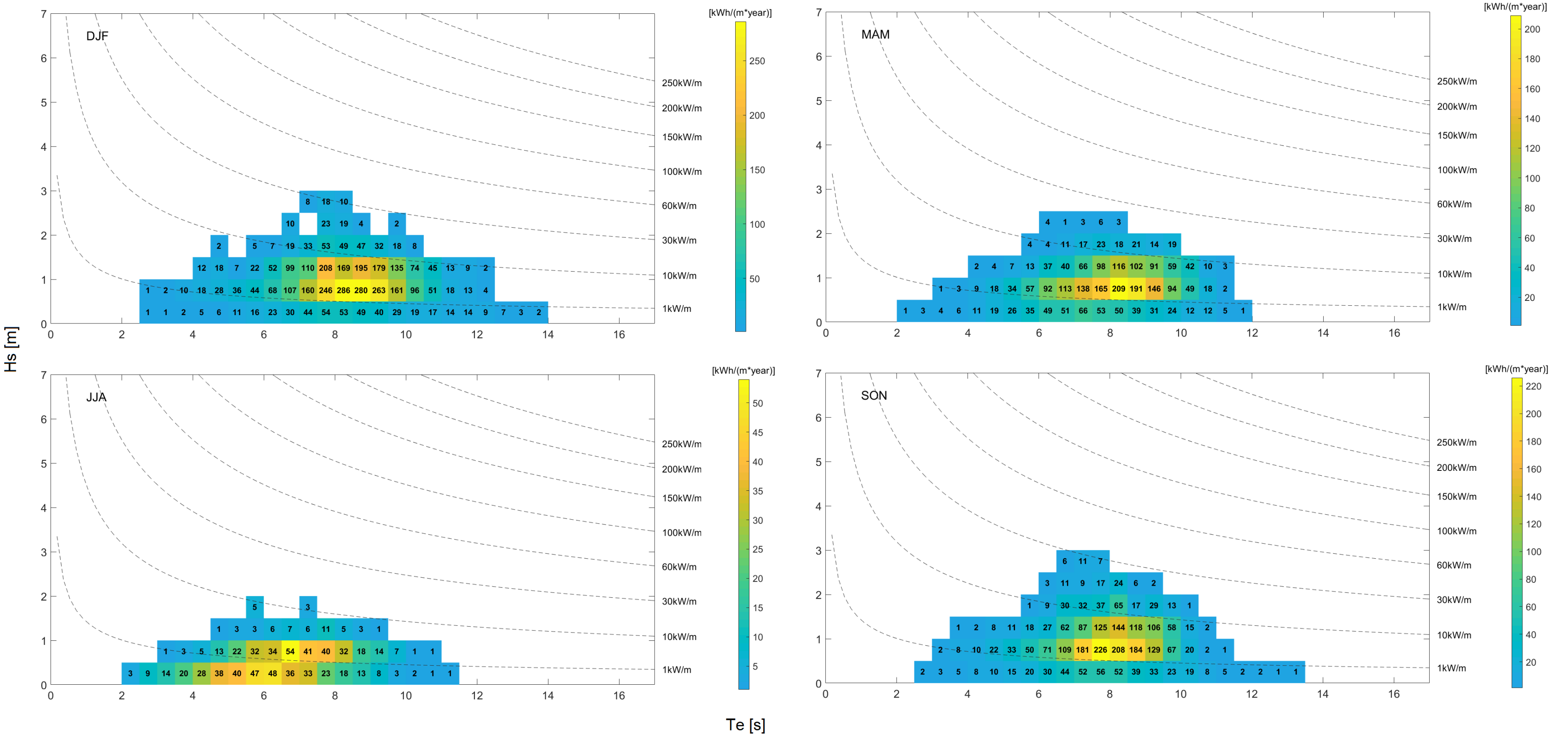

Figure 6.35: E_f in [kWh/(m*year)] for the different seasons at site B from SWAN 2007-2017. Dashed lines presenting lines of constant energy flux. Colours with numbers show the contribution of E_f to the total energy flux.

Chapter 7

Discussion

7.1 The use of SWAN in Sulafjorden and Breisundet

From the comparison of SWAN and the NPRA buoys, H_s from both data sets correlates well at all sites, again proving the good performance of SWAN, as other have stated (Ris et al. (1999) and Gusdal et al. (2010)). For high values SWAN underestimates H_s at site D, whereas overestimates at site A and B, in accordance with Christakos et al. (2020)'s result for the same area. Christakos et al. (2020) reasons this difference in the tuning of SWAN to coastal conditions. The swell impact in the area might have an impact as well on this feature. The correlation values for each compared variable decrease further into the fjord indicating some deviation related to modelling fjord systems. Different wind forcings have been applied to SWAN for Sulafjorden and Breisundet by Christakos et al. (2020). The conclusions from Christakos et al. (2020) show that the use of a high resolution wind field of 0.5 km (WRF 0.5) gives a good result for fjord systems which underpins the result for this thesis.

Regarding T_{m02}, figure 6.5, the difference in frequency range does play a part (Laing et al., 1998). The mentioned method of either applying a high-frequency tail to the buoy data or remove the high frequencies from the SWAN data is a good option to solve the problem. For this thesis T_{m02} is used in the wave energy flux calculation on the buoy data to compare the result to the SWAN E_f calculations. In the case where buoy measurement is the only available data, it is necessary to have correct T_{m02} values.

In the comparison of wave E_f for SWAN calculated with T_{m-10} and wave E_f for NPRA buoys calculated with T_{m02}, the buoys give higher result at almost all times (figure 6.28). For some measurements the deviation between SWAN and NPRA buoys is large. In order to estimate the wave power more precise for cases where the energy period is not available, more research is necessary. Longer time-series should be compared, and WPR for α values from spectrum information obtained by buoys should be looked into.

The characterisation of the wave climate both SWAN and the NPRA buoys show a combination of swell and wind sea domination, with swell dominating the mean wave direction. High values of H_s is experienced all the way into site B. This indicates that most part of the available wave energy is due to the incoming swell. Semedo et al. (2015) findings for the Nordic seas, corresponds well with this, Semedo et al. (2015) finds swell waves to be more prevalent in the Nordic Seas, and account for more of the incoming wave energy.

7.2 Energy Period

The correct estimation for T_e is T_{m-10}, this parameter can be calculated from the wave spectrum. In some cases, as for the NPRA buoys, this parameter is not accessible and estimates need to be made. Cahill and Lewis (2014) have investigated this issue and defined a new parameter namely the wave period ratio (WPR=α value), the ratio between the energy period T_{m-10} and the mean zero-crossing period T_{m02} or T_z. The reason for this investigation is due to the importance of correct calculations of wave energy available for wave energy converters. They discuss how the use of the frequently-employed wave period ratios is incorrect, and present more suitable ratios for the Bretschneider and JONSWAP theoretical spectra. For different spectrum shapes, different values for the WPR is provided and ranges from about 1.18 to 1.33. Goddijn-Murphy et al. (2015) uses the information from Cahill in the wave period calculation whereas Santo et al. (2016) uses the peak spectral wave period T_p for E_f calculations. T_p has higher variability and sensibility to changing sea states, producing additional errors. The decision of using T_{m02} in the search for the WPR to relate T_{m02} with T_{m-10} is therefore accepted for this thesis.

The spectra from SWAN is used to investigate the WPR for the area of Sulafjorden and Breisundet. None of the WPR at any of the site is as low as Cahill and Lewis (2014) gives. This is assumed to be due to the characteristics of the researched area and due to the weighting of the moments (equation 2.13 and 2.14). When the wave period changes inwards into the fjord the WPR also changes. This could be illustrated if a mean plot of T_{m02} was added to the research. From the case study, the most offshore point has the lowest WPR value of the available spectra sites with WPR=1.3. Due to the available spectra data own WPR ratios are used in the calculation of E_f for the NPRA buoys for the different sites, as this proves to give the most accurate wave energy flux. On another note, the WPR ratio fluctuates throughout the year as shown in figure 6.25, and as seen, it varies geographically. This impacts the wave energy approximation if calculating for a big area with changing sea states and characteristics. From the wave period analysis, it is also shown that an average WPR value approximates the wave energy flux in a good way if other measures are not available, but should be used with caution. As for this research the use of all the different alpha values the energy flux is overestimated compared to the calculation conducted with T_{m-10}. This is of course an issue with promising the energy production from a WEC, but being aware and accounting for the deviation would solve the issue.

7.3 The shallow-waterness of Sulafjorden and Breisundet

Equation 2.23 which calculates the results for the wave E_f for this thesis is valid for deep water. As Sulafjorden and Breisundet are fjord systems, it is easy to question if it is correct to use this equation for this area. As seen from the topography of Sulafjorden and Breisundet the area is quite deep at all sites. The use of equation 2.23 is therefore accepted. However, swells are dominating the area big parts of each year and if the bottom is felt by the incoming waves the related wave energy will be affected. This should be notified if further investigations on placing a WEC at these sites are being considered. Christensen et al. (2017) have investigated the ”shallow-waterness” of European coastal regions and found that a strong seasonal dependence affects when and where the water is considered shallow. In storm surges, the threshold between deep and shallow water takes place far into the open ocean.

7.4 Wave Energy Estimates

Comparing the wave energy flux estimates for Sulafjorden and Breisundet to the estimates of wave power in the North Sea it fits well with (Edenhofer et al., 2012)'s findings. Outside the Norwegian coast, the mean power is estimated to be about 35 kW/m. As Sulafjorden and Breisundet are stated as fjord systems a reduction from 35 kW/m in the open ocean to 10.6 kW/m at the most offshore point in Breisundet is acceptable. At the coast of Sweden the most offshore-lying points investigated by Waters et al. (2009) reaches 5.2 kW/m, whereas at the Balearic coast the highest value reaches 9.1 kW/m. Comparing these to the 10.6kW/m energy flux at site D, it seems reasonable to give this estimate for Breisundet.

7.5 Seasonal change and choice of WEC

The changing climate makes the winter-trend quite interesting to investigate, and as seen from the results in figure 6.17. A positive trend in H_s is found, a change of 0.25 metres for 10.5 years are found. This is in accordance with old and new literature, where the trend is slightly positive or non-existing for the relevant area (Bacon and Carter (1991) and Aarnes (2015)). Due to the latitude of the research sites, a seasonal trend in both H_s and E_f is expected and found. The standard deviation is large for all months as the variation in H_s from day to day to year to year is clear. It is difficult to state that the result is due to climate change as the time-series is only for 10.5 years, but a trend in the fjord system is found. The effect of the North Atlantic Oscillation (NAO) is not considered in this research but would have an impact on the winter swell and wind sea, and hence influence the available wave energy.

Annual variability in the wave energy flux is evident and increasing in general, this trend is confirmed by Santo et al. (2016) and Varlas et al. (2017). There is more uncertainty when estimating the wave resource for the winter months, in accordance with Neill and Hashemi (2013). If one of the sites should be chosen for WEC deployment, of course a lot needs to be considered and more research needs to be conducted. At site D the most energy is received, however, the variation is largest and this site experiences the highest waves at all times. At site A and B, the variation is more damped and the occurrence of higher waves are reduced. This indicates that it would be interesting to investigate how much of the theoretical wave power estimate could be converted to electrical energy at site B as it makes sense that here is the least impact from external forces. The wave direction at these sites is in general constant, mainly coming from one direction.

Chapter 8

Conclusions and Further Work

In this study data from SWAN driven by WRF wind and NPRA buoys from Sulafjorden and Breisundet are compared and analysed. The result is a description of the sea state with the related wave energy during the time from January 2007 to December 2018. The wave climate in this area is mostly swell-dominated with incidents of wind-driven domination, this is seen from the combined energy plots and the peak period T_p. Seasonal variations in H_s is found to be distinct, and have a higher impact at offshore than in the fjord. The analysis of the wave energy results in estimates of the annual mean theoretical wave energy for this area. Site D, Breisundet, has a potential of 10.6 kW per meter wave crest. At this site, the highest values of available wave energy is found. In Sulafjorden, at site A and B, the potential is respectively 4.1 kW/m and 1.2 kW/m. The variation in available wave energy has a seasonal trend for all sites throughout each year, with higher values during autumn/winter and lower for spring/summer. At site B the variation in wave energy is damped, indicating a more constant supply of energy throughout the year, with less extreme situations.

By comparing NPRA buoys and SWAN, the use of SWAN is validated and proved to be of great use in the area of Sulafjorden and Breisundet. Both the buoys and SWAN have limitations and errors, but these are not large enough to produce erroneous results. It proves to be of great usefulness having two sets originated from different sources in regards to validating and giving a more precise result for wave energy. The two different sources of data give the opportunity to investigate WPR in estimating the energy period. If T_e

is not available to calculate from the wave spectrum, the use of specified alpha values for T_{m02} for each site provide the best result on the wave energy flux. The α value increases further into the fjord indicating when working with both offshore and fjord systems one needs to be aware of the choice of the value. Using a constant α value fitted for open ocean might underpredict the energy flux at fjord sites. For this research α varies from 1.5 at site D to 1.9 at site B. Other fjords with different characteristics should be investigated in the same manner to provide a theory of why it varies like this and state some easy rules to follow when the need of α occurs.

The wave analysis of Sulafjorden and Breisundet and the corresponding wave energy estimated in this research contributes to a deeper understanding of wave energy calculations. It would be interesting to investigate the deployment of a WEC at site B due to the constant supply of wave energy and low seasonal variation found at this site, maybe as a part of a floating solar energy system or combined with fish farming. A longer time-series with wave data for the area should be analysed in the same manner to further improve the accuracy of the wave energy flux estimate and to account for a change in the trend. The impact of climate change on the wave energy flux could then be stated. The time-series should be long enough to be able to account for the effect of NAO on the wave energy potential as this would be necessary information if deploying a WEC. More observational buoys should be implemented at other locations on the west coast of Norway to analyse the wave energy potential to a greater extent, which also would contribute to monitoring the wave conditions at the coast.

Bibliography

Aarnes, O. J. (2015). *Extremes and Trends in Wave Climate. A regional and global study.* PhD thesis, The University of Bergen, Geophysical Institute, Bergen, Norway.

Aderinto, T. and Li, H. (2018). Ocean wave energy converters: Status and challenges. *Energies*, 11(5):1250.

Appavou, F., Brown, A., Epp, B., Gibb, D., Kondev, B., McCrone, A., Murdock, H. E., Musolini, E., Ranalder, L., Sawin, J. L., Seyboth, K., Skeen, J., and Sverrisson, F. (2019). *REN21 - 2019 Global Status Report*, pages 17–31. REN21.net.

Bacon, S. and Carter, D. J. (1991). Wave climate changes in the North Atlantic and North Sea. *International Journal of Climatology*, 11(5):545–558.

Booij, N., Ris, R. C., and Holthuijsen, L. H. (1999). A third-generation wave model for coastal regions: 1. model description and validation. *Journal of geophysical research: Oceans*, 104(C4):7649–7666.

Cahill, B. and Lewis, A. W. (2014). Wave period ratios and the calculation of wave power. *The 2nd Marine Energy Technology Symposium*, pages 1–10.

Christakos, K., Furevik, B. R., Aarnes, O. J., Breivik, Ø., Tuomi, L., and Byrkjedal, Ø. (2020). The importance of wind forcing in fjord wave modelling. *Ocean Dynamics*, 70(1):57–75.

Christensen, K. H., Carrasco, A., and Bidlot, J. R. (2017). The "shallow-waterness" of the wave climate in European coastal regions. *Ocean Science*, 13(4):589–597.

Dhanak, M. R. and Xiros, N. I. (2016). *Handbook of Ocean Engineering*, pages 15–27. Springer.

DNV-GL (2019). Energy Transition Outlook 2019. A global and regional forecast to 2050. *Energy Transition DNV GL*, pages 65–82, 114–126.

Edenhofer, O., Pichs-Madruga, R., Sokona, Y., Seyboth, K., Eickemeier, P., Matschoss, P., Hansen, G., Kadner, S., Schlömer, S., Zwickel, T., and Stechow, C. V. (2012). *Intergovernmental Panel On Climate Change - Summary for Policymakers. IPCC Special Report on Renewable Energy Sources and Climate Change Mitigation*, pages 41, 87–88. Intergovernmental Panel on Climate Change.

Falnes, J. (2002). *Lecture notes: Havbølgje-Energi.* Department of Physics, NTNU, Trondheim, Norway February 2002.

Folley, M., Whittaker, T., and Henry, A. (2005). The performance of a wave energy converter in shallow water. In *6th European Wave and Tidal Energy Conference, Glasgow, UK*, pages 133–140.

Fugro (2005). *Wavescan Buoy.* Fugro GEOS Company, Product Documentation.

Goddijn-Murphy, L., Míguez, B. M., McIlvenny, J., and Gleizon, P. (2015). Wave energy resource assessment with AltiKa satellite altimetry: A case study at a wave energy site. *Geophysical Research Letters*, 42(13):5452–5459.

Gusdal, Y., Carrasco, A., Furevik, B., and Saetra, O. (2010). Validation of the operational wave model wam and swan-2009. *Norwegian Meteorological Institute Report*, 18:2010.

Hasselmann, K., Barnett, T., Bouws, E., Carlson, H., Cartwright, D., Enke, K., Ewing, J., Gienapp, H., Hasselmann, D., Kruseman, P., et al. (1973). Measurements of wind-wave growth and swell decay during the joint north sea wave project (jonswap). *Ergänzungsheft 8-12.*

Hemer, M., Thornton, S., Stratigaki, V., Chanashyam, R., Molloy, S., and Wei, P. (2019). An Overview of Ocean Energy Activities in 2018. *The Executive Committee of Ocean Energy Systems*, pages 8–17, 105–106.

Holthuijsen, L. H. (2010). *Waves in oceanic and coastal waters*, pages 3–6, 13–15, 31–75, 120–130. Cambridge University Press.

Janssen, P. A., Breivik, Ø., Mogensen, K., Vitart, F., Balmaseda, M., Bidlot, J.-R., Keeley, S., Leutbecher, M., Magnusson, L., and Molteni, F. (2013). *Air-sea interaction and surface waves*, pages 1–2. European Centre for Medium-Range Weather Forecasts.

Laing, A. K., Gemmill, W., Magnusson, A. K., Burroughs, L., Reistad, M., Khandekar, M., Holthuijsen, L., Ewing, J. A., and Carter, D. J. T. (1998). *Guide to Wave Analysis*, volume 2(702), pages 1–14. Secretariat of the World Meteorological Organization.

Neill, S. P. and Hashemi, M. R. (2013). Wave power variability over the northwest european shelf seas. *Applied energy*, 106:31–46.

Norwegian-Mapping-Authority (2019). Norgeskart. `https://norgeskart.no/#!/?zoom=9&lon=34840.07&lat=6957574.96&project=norgeskart&layers=1008`, accessed on 2019-12-21.

Pecher, A. and Kofoed, J. P. (2017). *Handbook of ocean wave energy*, page 56. Springer London.

Pierson Jr, W. J. and Moskowitz, L. (1964). A proposed spectral form for fully developed wind seas based on the similarity theory of sa kitaigorodskii. *Journal of geophysical research*, 69(24):5181–5190.

Ponce de León, S., Orfila, A., and Simarro, G. (2016). Wave energy in the Balearic Sea. Evolution from a 29 year spectral wave hindcast. *Renewable Energy*, 85:1192–1200.

Ris, R., Holthuijsen, L., and Booij, N. (1999). A third-generation wave model for coastal regions: 2. verification. *Journal of Geophysical Research: Oceans*, 104(C4):7667–7681.

Ryszard, M. S. (1996). Ocean surface waves: their physics and prediction. *World scientific*, 11:37–39.

Santo, H., Taylor, P. H., Eatock Taylor, R., and Stansby, P. (2016). Decadal variability of wave power production in the North-East Atlantic and North Sea for the M4 machine. *Renewable Energy*, 91:442–450.

Semedo, A., Vettor, R., Breivik, Sterl, A., Reistad, M., Soares, C. G., and Lima, D. (2015). The wind sea and swell waves climate in the Nordic seas. *Ocean Dynamics*, 65(2):223–240.

Skamarock, W. C., Klemp, J. B., Dudhia, J., Gill, D. O., Barker, D. M., Wang, W., and Powers, J. G. (2008). A description of the advanced research wrf version 3. ncar technical note-475+ str. Citeseer.

SWAN-Team et al. (2009). Swan Scientific and Technical Documentation. *Delft University of Technology. Delft, Holland.*

The European Marine Energy Centre Ltd. (2009). *Assessment of Wave Energy Resource*, pages 1–36.

Thuesen, N. P., Thorsnæss, G., and Røvik, S. (2019). Norge. `https://snl.no/Norge`, accessed on 2019-12-16. Store Norske Leksikon.

Tolman, H. L. (1997). User manual and system documentation of wavewatch-iii version 1.15. National Oceanic and Atmospheric Administration NOAA.

Varlas, G., Christakos, K., Cheliotis, I., Papadopoulos, A., and Steeneveld, G. J. (2017). Spatiotemporal variability of marine renewable energy resources in Norway. *Energy Procedia*, 125:180–189.

WAMDI-Group (1988). The WAM model—A Third Generation Ocean Wave Prediction Model. *Journal of Physical Oceanography*, 18(12):1775–1810.

Waters, R., Engström, J., Isberg, J., and Leijon, M. (2009). Wave climate off the Swedish west coast. *Renewable Energy*, 34(6):1600–1606.

Waves4Power (2019). Timeline. `https://www.waves4power.com/demo-runde/`, accessed on 2019-12-16.